Interactions between Water Vapor, Potential Vorticity, and Vertical Wind Shear in Quasi-Geostrophic Motions: Implications for Rotational Tropical Motion Systems

ÁNGEL F. ADAMES[a,b]

[a] *Department of Climate and Space Science and Engineering, University of Michigan, Ann Arbor, Michigan*

(Manuscript received 9 July 2020, in final form 8 December 2020)

ABSTRACT: A linear two-layer model is used to elucidate the role of prognostic moisture on quasigeostrophic (QG) motions in the presence of a mean thermal wind ($\overline{u}_T$). Solutions to the basic equations reveal two instabilities that can explain the growth of moist QG systems. The well-documented baroclinic instability is characterized by growth at the synoptic scale (horizontal scale of ~1000 km) and systems that grow from this instability tilt against the shear. Moisture–vortex instability—an instability that occurs when moisture and lower-tropospheric vorticity exhibit an in-phase component—exists only when moisture is prognostic. The instability is also strongest at the synoptic scale, but systems that grow from it exhibit a vertically stacked structure. When moisture is prognostic and $\overline{u}_T$ is easterly, baroclinic instability exhibits a pronounced weakening while moisture vortex instability is amplified. The strengthening of moisture–vortex instability at the expense of baroclinic instability is due to the baroclinic ($\overline{u}_T$) component of the lower-tropospheric flow. In westward-propagating systems, lower-tropospheric westerlies associated with an easterly $\overline{u}_T$ advect anomalous moisture and the associated convection toward the low-level vortex. The advected convection causes the vertical structure of the wave to shift away from one that favors baroclinic instability to one that favors moisture–vortex instability. On the other hand, a westerly $\overline{u}_T$ reinforces the phasing between moisture and vorticity necessary for baroclinic instability to occur. Based on these results, it is hypothesized that moisture–vortex instability is an important instability in humid regions of easterly $\overline{u}_T$ such as the South Asian and West African monsoons.

KEYWORDS: Deep convection; Rossby waves; Monsoons; Moisture/moisture budget; Quasigeostrophic models; Tropical variability

1. Introduction

Large-scale (horizontal scale of ~1000 km) motion systems on Earth's atmosphere tend to be organized into vortices or waves. Decades of research onto these systems has shown that many of these grow from hydrodynamic instabilities. In the midlatitudes, where the Coriolis force is strong and motions are quasigeostrophic (QG), we observe large-scale Rossby waves and storm systems that grow from baroclinic instability (Eady 1949; Charney 1947; Phillips 1954; Bretherton 1966).

In the tropics, however, the weaker Coriolis force and resulting weak horizontal temperature gradients cause baroclinic instability to be less common. Nonetheless, some tropical motion systems have been hypothesized to grow from this instability. Among them are monsoon low pressure systems (MLPSs) and African easterly waves (AEWs).

The most notable similarity between the regions in which MLPSs and AEWs occur is that they are characterized by strong jets that exhibit strong easterly vertical shear ($\partial u/\partial z < 0$) (Burpee 1972; Roja Raman et al. 2009, 2011), although the depth of these jets differs in their respective regions. Because of this shear and the deep convection that is observed in association with these systems, it was thought that a variant of baroclinic instability that is modified by deep convection could explain their growth (Mass 1979; Salvekar et al. 1986; Krishnakumar et al. 1992). Baroclinic instability is characterized by geopotential and horizontal winds that are vertically tilted against the ambient shear (Eady 1949; Vallis 2017) (Fig. 1a).

Recent research into MLPSs and AEWs has put into question the central role that baroclinic instability plays in these waves. Cohen and Boos (2016) found that MLPSs exhibit a vertical structure that is inconsistent with baroclinic instability. Instead MLPSs exhibit an upright structure, akin to tropical depressions (Yoon and Chen 2005; Hunt et al. 2016; Clark et al. 2020). Similarly, Russell and Aiyyer (2020) found that AEWs exhibit a structure that is more upright than what would be observed if the waves were growing from moist baroclinic instability. Russell et al. (2020) found that organized convection maintains this upright structure, and is likely the main source of instability in AEWs.

Given that the mean state in the regions where both AEWs and MLPSs occur seems favorable for baroclinic instability, it

Denotes content that is immediately available upon publication as open access.

Supplemental information related to this paper is available at the Journals Online website: https://doi.org/10.1175/JAS-D-20-0205.s1.

[b] Current affiliation: Department of Atmospheric and Oceanic Sciences, University of Wisconsin–Madison, Madison, Wisconsin.

Corresponding author: Ángel F. Adames, angel.adamescorraliza@wisc.edu

Publisher's Note: This article was revised on 5 March 2021 to correct a typographical error in Table 2 that appeared when originally published.

DOI: 10.1175/JAS-D-20-0205.1

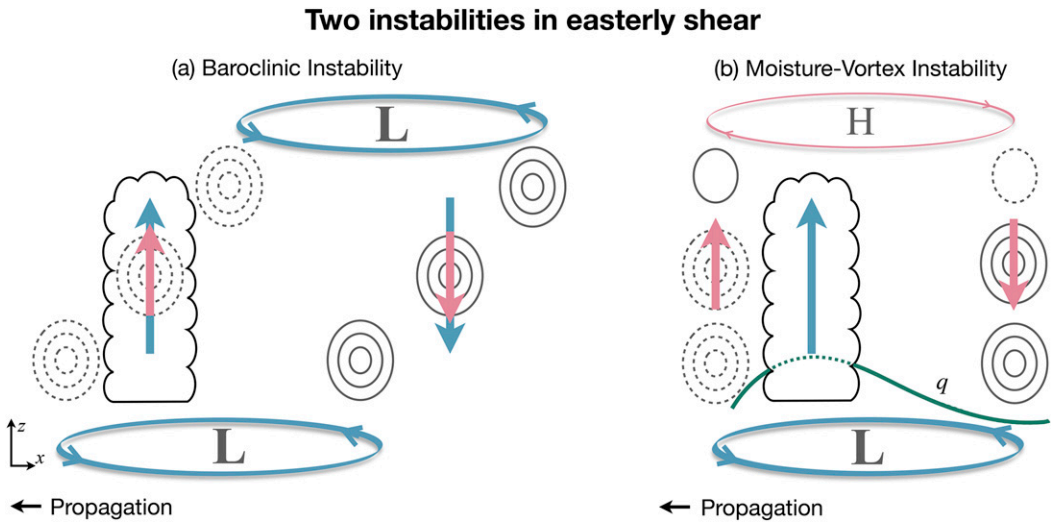

FIG. 1. Schematic describing the vertical structure of a wave that grows from the two instabilities discussed in this study in regions of easterly shear: (a) baroclinic instability and (b) moisture–vortex instability. Anomalous large-scale adiabatic lifting (subsidence) is shown as a upward (downward)-pointing pink arrow while anomalous ascent (descent) associated with enhanced (suppressed) convection is shown as a upward (downward)-pointing teal arrow. In (b) the moisture tendency qualitatively corresponds to the pink vertical arrow. Solid (dashed) contours depict anomalous poleward (equatorward) flow in the lower, mid-, and upper troposphere.

is perplexing that it may not be the main mechanism of growth in these systems. One possibility is that the mean state of the regions where these waves occur has properties that dampen baroclinic instability, favoring a different instability. But what mechanism could lead to this change? A possible answer to this question may be found in the numerical study by Lapeyre and Held (2004). They showed that when the atmosphere became humid, eddies driven by baroclinic instability were replaced by low-level vortices that resembled tropical cyclones. They argued that this occurrence is the result of a correlation between the lower tropospheric moisture and vorticity. Thus, it is possible that water vapor's interaction with convection and the large-scale circulation may fundamentally change the mechanisms by which tropical disturbances grow in the presence of vertical shear.

The role water vapor plays in modulating the occurrence and organization of tropical deep convection is well documented. For example, a humid free troposphere reduces the dilution that updrafts experience as they ascend (Kuo et al. 2017; Ahmed and Neelin 2018). The central role moisture has in tropical convection has led to the hypothesis that waves may exist where water vapor plays a central role in their dynamics (Sobel et al. 2001).

Some studies have hypothesized that moisture is important in MLPSs (Adames and Ming 2018b,a; Clark et al. 2020). Adames and Ming (2018a, AM18 from here on) hypothesized that the mechanism of growth in MLPSs involves interactions between the circulation, water vapor and convection. By solving a system of shallow water equations with prognostic moisture and a simple convective adjustment scheme, AM18 found that vortices can grow from moisture–vortex instability (Fig. 1b). In this instability the anomalous meridional winds advect moisture, resulting in a moisture tendency. The moisture anomalies lag the moisture tendency and are shifted toward the center of the vortex (Fig. 1b). The enhanced convection that results from the higher moisture content intensifies the vortex through vortex stretching. While AM18 show that MLPSs could potentially grow from moisture–vortex instability, they did not take into account the large vertical wind shear that is usually observed in the South Asian monsoon.

In this study, we will expand upon AM18's framework by applying it to a two-layer QG model. Such models have been used to understand baroclinic instability (Phillips 1954; Bretherton 1966; Vallis 2017) and to simulate the midlatitude circulation (Pavan and Held 1996; Lapeyre and Held 2004). They have also been used to understand the dynamics of MLPSs and AEWs (Aravequia et al. 1995; Salvekar et al. 1986; Grist et al. 2002). However, the impact that a prognostic moisture equation may have in a linear two-layer QG system has not been studied in detail. We will show that including a prognostic moisture equation significantly modulates the dynamics of waves that propagate in the presence of a thermal wind. Specifically, it weakens baroclinic instability in regions of easterly shear while favoring moisture–vortex instability. The results of this study may explain why baroclinic instability is not the dominant mechanism for growth in MLPSs, and may support recent work on the growth of AEWs.

This study is structured as follows. The next section describes the moist two-layer QG model. Wave solutions to the system of equations are obtained in section 3. Section 4 discusses the wave solutions that arise when moisture is diagnosed from the large-scale wind fields. Section 5 discusses how these solutions change when a prognostic moisture equation is included. Section 6 discusses how baroclinic instability is modified when prognostic moisture is included. A synthesis and discussion of the main findings of this study is offered in section 7. Concluding remarks are given in section 8.

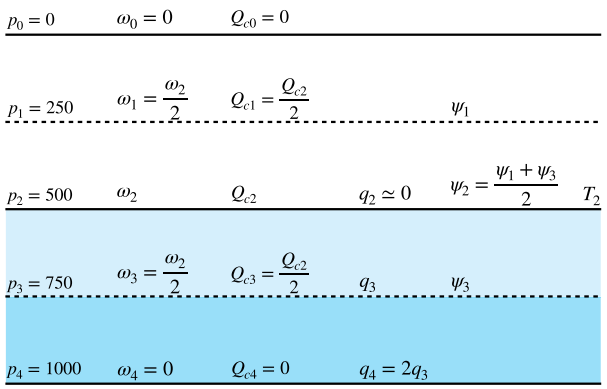

FIG. 2. Schematic describing the vertical arrangement of variables used in the two-layer moist QG model. The shading indicates the specific humidity in the layer.

2. Two-layer quasigeostrophic model with prognostic moisture

a. Basic equations

Our analysis is based on a two-layer linear QG model with prognostic moisture. The layout of the model closely follows Holton and Hakim (2012) and is described in Fig. 2. The main variables are shown in Table 1. Constants and their values are shown in Table 2. The lower tropospheric layer is bounded by the 1000 and 500 hPa surfaces. We will assume that all moisture is located within this layer. The upper tropospheric layer is bounded by the 0 and 500 hPa layer. Vertical motion is assumed to be a maximum in the 500 hPa layer, and vanishes at the 1000 and 0 hPa surfaces. It would be more realistic to have an upper boundary at 100 hPa instead of 0 since vertical velocities in the tropics approximately vanish at this layer. However, we keep the top at 0 hPa so that readers can directly compare the results of this study with chapter 7 of Holton and Hakim (2012). Our results are not sensitive to the choice of an upper bound between 100 and 0 hPa. The validity of the QG approximation for AEWs and MLPSs is discussed in section a of the appendix.

Because the vertical velocity is a maximum in the midtroposphere, it follows that the associated low-level convergence and upper-level divergence result in winds and geopotential field components that exhibit a "first baroclinic" structure; i.e., the fields exhibit a reversed polarity in the lower and upper troposphere. Baroclinic disturbances are characterized by temperature perturbations that are related to the geopotential through hydrostatic balance. We can write this relationship in the two-layer model as

$$\frac{\Phi_3 - \Phi_1}{\ln(p_3/p_1)} = -R_d T_2, \tag{1}$$

where R_d is the dry gas constant, Φ is the geopotential, and T is the temperature. The subscripts describe the layer of the field following Fig. 2.

The planetary vorticity is linearized with respect to a reference latitude by applying the β-plane approximation:

TABLE 1. The main variables and definitions used in this study.

Variable	Description	Units
ψ	Streamfunction	$m^2\,s^{-1}$
Φ	Geopotential	$m^2\,s^{-2}$
T	Temperature	K
ζ	Relative vorticity	s^{-1}
$\mathbf{v}$	Horizontal wind vector	$m\,s^{-1}$
$\overline{u}_T$	Mean thermal wind	$m\,s^{-1}$
$\overline{u}_B$	Mean barotropic wind	$m\,s^{-1}$
D	Horizontal divergence	s^{-1}
P	Precipitation rate	$J\,kg^{-1}$
q	Specific humidity	—
τ_c	Convective moisture adjustment time scale	s
q_d	Dry potential vorticity (PV)	s^{-1}
q_m	Moist-component PV	s^{-1}
q_G	Gross PV	s^{-1}
s	Dry static energy (DSE)	$J\,kg^{-1}$
Q_c	Convective heating	$J\,kg^{-1}\,s^{-1}$
ω'	Vertical pressure velocity anomaly	$Pa\,s^{-1}$
ω^*	Wave frequency	s^{-1}
ω	Wave frequency relative to $\overline{u}_B$	s^{-1}
ω_0	Relative wave frequency when $\tau_c = 0$	s^{-1}
k	Zonal wavenumber	m^{-1}
c_p	Phase speed relative to $\overline{u}_B$	$m\,s^{-1}$
$\overline{M}_s$	Mean gross dry stability	$J\,m^{-2}$
$\overline{M}_q$	Mean gross moisture stratification	$J\,m^{-2}$
m	Normalized gross moist stability	—
β_T	Meridional temperature gradient	$m^{-1}\,s^{-1}$
β_q	Meridional moisture gradient	$m^{-1}\,s^{-1}$
α_ψ	Phase angle between ψ'_T and ψ'_B	—
α_P	Phase angle between ψ'_T and P'	—
δ	Component of ω associated with baroclinic instability	s^{-1}
$\mathfrak{B}_d$	Term associated with dry baroclinic instability	$s^{-2}\,m^{-3}$
$\mathfrak{B}_m$	Term associated with moist baroclinic instability	$s^{-2}\,m^{-3}$
$\mathfrak{M}$	Moisture–vortex interaction term	—

$$f = f_0 + \beta y, \tag{2}$$

where f_0 and $\beta = df/dy$ are the planetary vorticity and the meridional planetary vorticity gradient evaluated at a reference latitude, respectively. Since we are interested in motions that occur in the "outer tropics" (10°–30°N/S), we will assume a value of f_0 of $4 \times 10^{-5}\,s^{-1}$, a value that corresponds to 16°N.[1]

We can express many of the field variables in terms of a geostrophic streamfunction ψ. In the QG approximation, ψ is linearly related to Φ:

$$\psi = \Phi f_0^{-1}. \tag{3}$$

[1] The planetary vorticity in the northern outer tropics (10°–30°N) ranges from 2.5 to $7.2 \times 10^{-5}\,s^{-1}$. While these values smaller than those of the midlatitudes, they are not small enough to invalidate the QG approximation, though it is indeed less robust than in the midlatitudes.

TABLE 2. Constants used in this study and their value.

Variable	Description	Value	Units
C_p	Specific heat capacity of dry air	1004	J kg^{-1} K^{-1}
R_d	Gas constant of dry air	287	J kg^{-1} K^{-1}
L	Latent heat of vaporization	2.5×10^6	J kg^{-1}
g	Gravitational acceleration	9.8	m s^{-2}
Δp	Pressure thickness of the layer	500	hPa
f_0	Planetary vorticity at 16°N	4×10^{-5}	s^{-1}
β	Gradient of planetary vorticity	2.2×10^{-11}	m^{-1} s^{-1}
c	Free gravity wave phase speed	53	m s^{-1}
k_d	Inverse of the Rossby radius of deformation	7.5×10^{-7}	m^{-1}

The horizontal wind $\mathbf{v} = u\mathbf{i} + v\mathbf{j}$ can be obtained from ψ as follows:

$$u = -\frac{\partial \psi}{\partial y}, \quad v = \frac{\partial \psi}{\partial x}, \tag{4}$$

where $\mathbf{i}$ and $\mathbf{j}$ are the zonal and meridional unit vectors. The vertical component of the relative vorticity (ζ) is written as

$$\zeta = \nabla_h^2 \psi, \tag{5}$$

where $\nabla_h^2 = \partial_x^2 + \partial_y^2$ is the horizontal Laplacian.

We will assume that both convective heating Q_c and vertical motion ω exhibit a single vertical structure in which they attain a maximum amplitude at 500 hPa (layer 2), and become zero at the top and bottom boundaries. At the 750 hPa layer, Q_{c3} and ω_3 can be obtained by interpolating between the 0 and 500 hPa layers $\omega_3 = (\omega_4 + \omega_2)/2$. Since ω vanishes in the top and bottom boundaries, it follows that

$$\omega_3 = \frac{\omega_2}{2}. \tag{6}$$

The same procedure can be done to obtain ω_1 and Q_{c1}. To relate the horizontal divergence $D = \nabla \cdot \mathbf{v}$ to ω, we invoke mass continuity in each discrete layer. Since $\omega = 0$ at the top and bottom boundaries, we can write the divergence in layers 1 and 3 as

$$D_1' = -\frac{\omega_2}{\Delta p}, \quad D_3' = \frac{\omega_2}{\Delta p}. \tag{7}$$

We will decompose the main variables into mean state and perturbation components, denoted by an overbar and a prime, respectively:

$$\psi(x, y, t) = \overline{\psi}(y) + \psi'(x, t). \tag{8}$$

As in Holton and Hakim (2012), and Vallis (2017), we define $\overline{\psi}$ as only varying in the meridional direction while ψ' varies zonally and temporally. Assuming that the mean zonal wind is a constant in space and time, we can express the mean streamfunction as

$$\overline{\psi}_1 = -\overline{u}_1 y, \tag{9a}$$

$$\overline{\psi}_3 = -\overline{u}_3 y. \tag{9b}$$

The same assumption is made for the lower-tropospheric water vapor (q_3) and midtropospheric temperature (T_2), i.e.,

$$q_3(x, y, t) = \overline{q}_3(y) + q_3'(x, t), \tag{10a}$$

$$T_2(x, y, t) = \overline{T}_2(y) + T_2'(x, t). \tag{10b}$$

We can combine Eqs. (1), (3), and (9) to obtain the thermal wind equation:

$$\frac{\partial T_2}{\partial y} = \frac{f_0}{R_d} \frac{\overline{u}_3 - \overline{u}_1}{\ln(p_3/p_1)}, \tag{11}$$

which shows that the mean meridional temperature gradient is constant in space and time. We will test the sensitivity of the wave solutions to the mean thermal wind by varying the amplitude of the meridional temperature gradient from 0 to ±5 K (1000 km)$^{-1}$. For simplicity, we will assume that the mean meridional moisture gradient is also a constant:

$$\frac{\partial \overline{q}_3}{\partial y} = \text{constant}. \tag{12}$$

To test the sensitivity of the wave solutions to the meridional moisture gradient, we will vary its amplitude from 0 to ±1.2 g kg^{-1} (1000 km)$^{-1}$. The change in moisture with increasing latitude is much smaller than $\overline{q}_3$, which is on the order of 10 g kg^{-1}.

We are assuming that perturbations are only in the zonal plane since instabilities that involve quasigeostrophic motions tend to prefer the longest meridional scales (see, e.g., Vallis 2017), even when prognostic moisture is included (AM18).

With these approximations and definitions, we can write our upper- and lower-tropospheric vorticity, midtropospheric temperature, and lower-tropospheric moisture equations as

$$\left(\frac{\partial}{\partial t} + \overline{u}_1 \frac{\partial}{\partial x}\right) \zeta_1' = -v_1' \beta - f_0 D_1', \tag{13a}$$

$$\left(\frac{\partial}{\partial t} + \overline{u}_3 \frac{\partial}{\partial x}\right) \zeta_3' = -v_3' \beta - f_0 D_3', \tag{13b}$$

$$\left(\frac{\partial}{\partial t} + \overline{u}_2 \frac{\partial}{\partial x}\right) C_p T_2' = -v_2' \frac{\partial C_p \overline{T}_2}{\partial y} - \omega_2' \frac{\Delta \overline{s}}{\Delta p} + Q_{c2}', \tag{13c}$$

$$\left(\frac{\partial}{\partial t} + \overline{u}_3 \frac{\partial}{\partial x}\right) L q_3' = -v_3' \frac{\partial L \overline{q}_3}{\partial y} - \omega_3' \frac{\Delta L \overline{q}}{\Delta p} - \frac{g}{\Delta p} L P', \tag{13d}$$

where $\Delta s = \overline{s}_3 - \overline{s}_1 < 0$ is the vertical change in dry static energy ($s = C_p T + \Phi$), $\Delta Lq = \overline{L} q_4 - \overline{L} q_2 > 0$ is the vertical change in latent energy between 1000 and 500 hPa, $\Delta p = p_3 - p_1$, and g is the gravitational acceleration

The system of equations in Eq. (13) are the same equations used to describe baroclinic instability in textbooks (Holton and Hakim 2012; Vallis 2017). They differ in that a linearized moisture equation is included and that convective heating is included in the thermodynamic equation. With the addition of moisture, the two-layer model is reminiscent to those employed by Lapeyre and Held (2004), and Lambaerts et al. (2012), except that this model is linear.

b. Convective parameterization

The definitions given by Eqs. (1)–(7) are sufficient to solve the dry two-layer QG model discussed in chapter 7 of Holton and Hakim (2012). However, our study includes deep moist convection and a prognostic moisture equation. The representation of convection and the way it couples Eq. (13d) to Eqs. (13a)–(13c) will be key to the main findings of this study.

To facilitate the discussion on the convective parameterization, we will decompose ω_2' into an adiabatic and diabatic component, denoted by the subscript a and Q, respectively:

$$\omega_2' = \omega_a' + \omega_Q'. \tag{14}$$

Both ω_a' and ω_Q' can be diagnosed from the QG omega equation, as was done by Nie and Sobel (2016) and Murthy and Boos (2020). However, we will focus on the thermodynamic equation [Eq. (13c)] in order to maintain the discussion simple. The adiabatic component of the vertical velocity is due to the temperature tendency and temperature advection:

$$\omega_a' \equiv -\frac{\Delta p C_p}{\Delta \bar{s}}\left(\frac{\partial T_2'}{\partial t} + \overline{u}_2\frac{\partial T_2'}{\partial x} + v_2'\frac{\partial \overline{T}_2}{\partial y}\right), \tag{15}$$

while the diabatic component can be defined as the component that exactly satisfies the weak temperature gradient approximation (WTG) (Sobel et al. 2001):

$$\omega_Q' \equiv \frac{\Delta p}{\Delta \bar{s}} Q_{c2}'. \tag{16}$$

Many previous studies diagnose ω_Q' in terms of ω_a' ($\omega_Q' \propto \omega_a'$) (Mak 1982; Sanders 1984), leading to the in-phase relationship shown in Fig. 1a. This type of diagnosis is appropriate for extratropical motions, where adiabatic lifting is strong and can create broad regions of stratiform cloudiness. For the tropical disturbances considered here, ω_a' and ω_Q' are not in phase (see Fig. 12 in Adames and Ming 2018b). In the tropics, the main source of diabatic heating is deep cumulus convection, whose buoyancy is sensitive to the thermodynamic environment rather than the large-scale ascent (Brown and Zhang 1997; Mapes 2000; Ahmed and Neelin 2018). Adames and Ming (2018b) showed that anomalous precipitation in simulated MLPSs is more closely in phase with anomalous water vapor, rather than large-scale lifting (their Fig. 5). A recent study by Nie et al. (2020) showed that rainfall rates from deep convection (ω_Q) are much larger than the rates obtained from large-scale forcing (ω_a) in the Asian and African monsoons (their Fig. 2).

Simplified models of the tropics often parameterize the deep convection by employing a convective adjustment scheme such as the Betts–Miller scheme (Betts and Miller 1986). In these schemes, convection adjusts the temperature and moisture back to a reference profile. Clark et al. (2020) showed that MLPSs with realistic structures can be simulated by representing convection with a Betts–Miller scheme. We will use a similar parameterization to that used by Clark et al. (2020), but only include the modulation of convection by water vapor, as in other simplified studies of tropical motion systems (Sobel et al. 2001; Fuchs and Raymond 2005; AM18). Thus, we will express Q_{c2}' as

$$Q_{c2}' \simeq \frac{Lq_3'}{\tau_c}, \tag{17}$$

where τ_c is the convective moisture adjustment time scale. It is estimated to range between 2 and 12 h (Betts 1986; Neelin and Zeng 2000; Bretherton et al. 2004; Sugiyama 2009). We will use a value of 6 h when applicable. Sensitivity tests using various values of τ_c yield results similar to those discussed by AM18. The main findings of this study are the same regardless of whether τ_c is 2 or 12 h.

Equation (17) is similar to Eq. (12) in Ahmed et al. (2020), but without the inclusion of temperature. Ahmed et al. (2020) found that the observed relationship between diabatic heating and the buoyancy of an entraining plume can be written in terms of lower-tropospheric temperature and moisture: $Q_{c2}' = h_4'/\tau_b + Lq_3'/\tau_q - C_pT_3'/\tau_t$, where τ_q, τ_t, and τ_b are sensitivity time scales akin to τ_c, and $h_4 = C_pT_4 + Lq_4$ is the boundary layer moist enthalpy. While their relationship is empirical, it summarizes the physical processes that lead to precipitation, that is, deep convection occurs when the atmospheric lapse rate is sufficiently unstable to convection and the troposphere sufficiently humid so that updrafts dilute less. If we ignore temperature and assume that $q_4 = 2q_3$, we can show that $\tau_c = \tau_q\tau_b/(2\tau_q + \tau_b)$. While we recognize that the temperature anomalies may play a role in determining the distribution of precipitation in systems like MLPSs and AEWs, focusing on water vapor will yield simpler equations with solutions that are easier to interpret. However, we recognize that the exclusion of temperature's role in Q_{c2}' may be a limitation of this study.

The anomalous precipitation P can be related to the column-integrated convective heating Q_c following Yanai et al. (1973):

$$LP' = \frac{\Delta p}{g} Q_{c2}'. \tag{18}$$

Equation (18) will allow us to combine Eqs. (13c) and (13d) into a single equation for moist enthalpy, as discussed in the following subsection.

It is worth pointing out that the equations describing vertical velocity in this study do not apply the WTG approximation strictly. Rather, by allowing ω_a to be nonzero, we are applying what is referred to as a "relaxed" WTG approximation (Raymond and Zeng 2005). While the WTG approximation is generally considered reasonable in MLPSs and AEWs (Adames and Ming 2018b; Hannah and Aiyyer 2017), the relaxed WTG approximation allows for the temperature tendency and the temperature advection to play a role in the

dynamics of the waves analyzed here. Their contributions to Eq. (13c) may be small, but they may play an important role in the convective coupling of these systems.

c. *Equations for barotropic vorticity and QG potential vorticity*

With the approximations and assumptions discussed in sections 2a and 2b, we can reduce the number of variables in Eq. (13) to three. To reduce our four basic equations in Eq. (13) to three, we will eliminate the thermodynamic equation by defining the baroclinic and barotropic streamfunctions, ψ'_T and ψ'_B, respectively, as

$$\psi'_T = (\psi'_1 - \psi'_3)/2, \tag{19a}$$

$$\psi'_B = (\psi'_1 - \psi'_3)/2, \tag{19b}$$

and defining the mean thermal (baroclinic) and barotropic zonal winds as

$$\overline{u}_T = (\overline{u}_1 - \overline{u}_3)/2, \tag{20a}$$

$$\overline{u}_B = (\overline{u}_1 + \overline{u}_3)/2. \tag{20b}$$

Positive values of $\overline{u}_T$ indicate westerly shear and positive ψ'_T indicate positive ψ' anomalies in the upper troposphere.

Using Eq. (19), we can combine Eqs. (13a)–(13c) to obtain an equation for the barotropic vorticity and for the QG potential vorticity (q_d). We can also combine Eqs. (13c) and (13d) following AM18 to obtain an equation for the moist enthalpy ($C_pT + Lq$). The resulting equations are written as

$$\frac{\overline{D}_h \zeta'_B}{Dt} = -v'_B\beta - \overline{u}_T \frac{\partial \zeta'_T}{\partial x}, \tag{21a}$$

$$\frac{\overline{D}_h q'_d}{Dt} = -v'_T\beta - v'_B\beta_T - \overline{u}_T \frac{\partial \zeta'_B}{\partial x} - \frac{f_0}{\overline{M}_s} LP', \tag{21b}$$

$$\frac{\overline{D}_h q'_m}{Dt} = v'_T\beta_q - v'_B\left(\beta_T + \beta_q\right) + \overline{u}_T \frac{f_0\tau_c}{\overline{M}_q}\frac{\partial P'}{\partial x} - \frac{mf_0}{\overline{M}_q} LP', \tag{21c}$$

where

$$\frac{\overline{D}_h}{Dt} = \frac{\partial}{\partial t} + \overline{u}_B \frac{\partial}{\partial x} \tag{22}$$

is the horizontal material derivative for a disturbance propagating relative to a mean barotropic flow ($\overline{u}_B$). The dry baroclinic PV anomaly is written as

$$q'_d = \zeta'_T - k_d^2 \psi'_T, \tag{23a}$$

where

$$k_d = \frac{f_0}{c} \tag{23b}$$

is the inverse of the Rossby radius of deformation and

$$c = \left(\frac{gR_d\overline{M}_s}{2p_2C_p}\right)^{1/2} \tag{23c}$$

is the phase speed of free gravity waves.

The moist enthalpy is written in the form of a "moist equivalent" potential vorticity, that is, the enthalpy is written in units of s^{-1}:

$$q'_m = \frac{f_0\tau_c}{\overline{M}_q} P' + k_d^2 \psi'_T. \tag{23d}$$

Note that the definition of q'_m used here differs from that in AM18 in the sign of the second term because we have defined ψ'_T to be positive for positive upper-tropospheric ψ'. AM18 defined ψ'_T so that it is positive for positive lower-tropospheric ψ'.

In converting Eq. (13) into Eq. (21) we have defined new variables and constants. The constants $\overline{M}_q$ and $\overline{M}_s$ are the gross moisture stratification and gross dry stability (Yu et al. 1998; Adames and Kim 2016), respectively defined as

$$\overline{M}_q = L\Delta\overline{q}\frac{\Delta p}{2g}, \tag{24a}$$

$$\overline{M}_s = -\Delta\overline{s}\frac{\Delta p}{g}. \tag{24b}$$

From Eq. (24) we can see that $\overline{M}_q$ and $\overline{M}_s$ are the mass-weighted vertical changes in Lq and s, respectively. We also have defined m as the normalized gross moist stability (NGMS):

$$m = \frac{\overline{M}_s - \overline{M}_q}{\overline{M}_s}. \tag{25}$$

Note that we have opted for the use of lowercase m for the NGMS since it is the same definition given by Neelin and Held (1987), except that it is divided by $\overline{M}_s$. The NGMS m can be interpreted as the moist static stability of the column per unit of dry static stability. It has a value of unity in a dry atmosphere, and can be near zero or negative in humid atmospheres. We will use a value of 0.2 in this study, which is close to the NGMS values documented in observations (Sobel et al. 2014; Inoue and Back 2015). The sensitivity of the wave solutions analyzed in this study to variations in m is shown in the online supplementary material.

In Eq. (21) we also define β_q as the mean meridional moisture gradient,

$$\beta_q = \frac{2f_0}{\Delta\overline{q}}\frac{\partial\overline{q}_3}{\partial y}, \tag{26a}$$

and β_T as the mean meridional temperature gradient,

$$\beta_T = -\overline{u}_T k_d^2. \tag{26b}$$

These variables are defined so they are in the same units as β, i.e., $m^{-1}\,s^{-1}$, following AM18.

With the variables and constants in Eq. (21) defined, we will now discuss the processes that lead to the evolution of the three main variables. The evolution of ζ'_B is driven by the advection of planetary vorticity by v'_B and advection of ζ'_B by $\overline{u}_T$.

The processes that lead to the evolution of q'_d relative to the mean barotropic flow [rhs in Eq. (21b)] are

- advection of planetary vorticity by v'_T,
- advection of mean temperature by v'_B,
- advection of ζ'_B by $\overline{u}_T$,
- vortex stretching of planetary vorticity by the anomalous divergence in anomalous convection.

The first three processes are those also found in studies of dry baroclinic instability, while the last term is the result of moist convection. It is worth noting that the last rhs term in Eq. (21b) can exist even if moisture is not prognostic. However, when moisture is prognostic, it is this term that is key in the coupling of the moisture anomalies with q'_d and ζ'_B. The impact that having a prognostic moisture equation without convection is discussed in the supplementary material.

The processes that lead to the evolution of q'_m relative to the mean barotropic flow [rhs in Eq. (21c)] are

- advection of mean moisture by v'_T,
- advection of mean moist enthalpy by v'_B,
- advection of the moisture anomalies by $\overline{u}_T$,
- vertical advection of moist static energy by the vertical motion in anomalous convection.

Equations (21b) and (21c) contain four terms on the right hand side that mirror one another. However, even though Eqs. (21b) and (21c) are similar, they do not necessarily contribute equally to the evolution of a moist wave.

d. Gross potential vorticity

We can understand the relative contributions of Eqs. (21b) and (21c) to the evolution of a moist wave by following AM18 and combining the equations to obtain the "gross" PV:

$$q'_G = (1-m)q'_m - mq'_d. \tag{27}$$

The evolution of q'_G is given by

$$\frac{\overline{D}_h q'_G}{Dt} = (1-m)\left[v'_T\beta_q - v'_B\left(\beta_q+\beta_T\right) + \overline{u}_T\frac{f_0\tau_c}{\overline{M}_q}\frac{\partial P'}{\partial x}\right] - m\left[-v'_T\beta + v'_B\beta_T - \overline{u}_T\frac{\partial \zeta'_B}{\partial x}\right]. \tag{28}$$

As discussed by AM18, Eq. (28) describes the relative importance of dry and moist processes to the evolution of a moist wave. The dry processes are multiplied by $-m$ while the moist processes are multiplied by $1-m$. When $m \to 1$, the atmosphere is dry and moist processes play no role in the evolution of the wave. Conversely, when $m \to 0$, moist processes govern the evolution of the wave while dry processes play no role. It is worth noting that the thermal wind (both as $\overline{u}_T$ and β_T) contributes to both dry and moist processes, indicating that it plays a role in the evolution of the wave regardless of the value of m.

3. Wave solutions

a. Dispersion relation

The system of equations in Eq. (21) can be solved by assuming that they can be described by a wave of the following form:

$$\psi'_T = \psi'_{T0}\exp(ikx - i\omega^* t), \tag{29a}$$

$$\psi'_B = \psi'_{B0}\exp(ikx - i\omega^* t), \tag{29b}$$

$$P' = P'_0\exp(ikx - i\omega^* t), \tag{29c}$$

where k is the zonal wavenumber, ω^* is the wave frequency, and ψ'_{T0}, ψ'_{B0}, and P'_0 are the initial amplitudes.

Because the only role of $\overline{u}_B$ is to advect the wave, it will be convenient to define the wave frequency relative to it:

$$\omega = \omega^* - \overline{u}_B k. \tag{30}$$

This definition will allow us to simplify the equations that follow without losing any physical insight. With this simplification, we can solve Eq. (21) by substituting the field variables with their solutions in Eq. (29). After substitution, we can find nontrivial solutions to Eq. (21) if the determinant of the coefficients ψ'_{T0}, ψ'_{B0}, and P'_0 is zero. By finding the determinant we obtain a cubic dispersion relation of the form

$$[m - i\tau_c(\omega + \overline{u}_T k)]\mathfrak{B}_d + (1-m)\mathfrak{B}_m = 0, \tag{31a}$$

where

$$\mathfrak{B}_d = \omega^2 k\left(k^2 + k_d^2\right) + \omega\beta\left(k_d^2 + 2k^2\right) + \beta^2 k + \overline{u}_T^2 k^3\left(k_d^2 - k^2\right) \tag{31b}$$

are the terms that define the counterpropagating waves that lead to dry baroclinic instability, and

$$\mathfrak{B}_m = \omega^2 k k_d^2 + \omega\left(\beta k_d^2 + 2\beta_q k^2\right) + 2\beta\beta_q k - \overline{u}_T k^3\beta_m \tag{31c}$$

are the terms that define the counterpropagating waves that lead to moist baroclinic instability. Equation (31) is the general form of the dispersion relation for moist QG waves in the two-layer model employed here. It will be used both to elucidate the propagation and growth of these waves and to evaluate approximate solutions that will be discussed in subsequent sections. Additional discussion on $\mathfrak{B}_d$ and $\mathfrak{B}_m$ is offered in section b(2) of the appendix.

b. Polarization relations and phase relations

For a given zonal distribution of ψ'_B, the polarization relations for ψ'_T and P' take the following form:

$$\psi'_T = \frac{\beta + \omega k}{\overline{u}_T k^2}\psi'_B, \tag{32a}$$

$$P' = \frac{i\overline{M}_q\left[\left(k_d^2\omega + \beta_q k\right)\psi'_T - \left(\beta_q + \beta_T\right)k\psi'_B\right]}{f_0\left[m - i\tau_c(\omega + \overline{u}_T k)\right]}. \tag{32b}$$

The polarization relations in Eq. (32) show that the barotropic and baroclinic streamfunctions couple only when $\overline{u}_T \neq 0$, consistent with previous studies (Phillips 1954; Wang and Xie 1996). Equation (32b) shows that P' scales in proportion to $\overline{M}_q$, i.e., P' is greater in a humid mean state. Both ψ'_T and ψ'_B contribute to P'.

A special case of Eq. (32b) can be obtained when $\beta_q = 0$, which can be written as

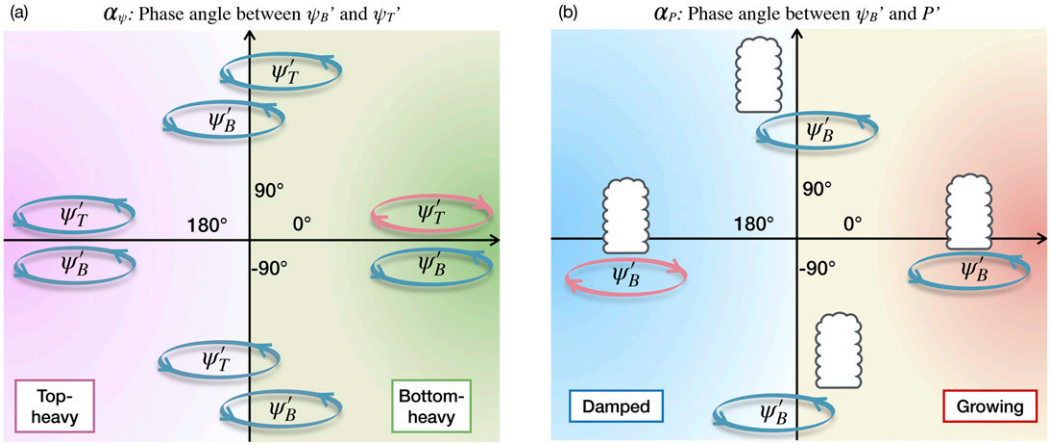

FIG. 3. Schematic describing (a) the phasing between ψ'_T and ψ'_B according to α_ψ and (b) the phasing between ψ'_B and P' according to α_P. Regions in (a) where the resulting structure is top-heavy (wave signature stronger in the upper troposphere) is shown as purple while the region where the structure is more bottom-heavy is shown as green. Regions in (b) where the convection has an in-phase component with the midtropospheric cyclone (anticyclone) is shown in red (blue).

$$P' \simeq \frac{i\overline{M}_q k_d^2 \left(\omega\psi'_T + \overline{u}_T k\psi'_B\right)}{f_0\left[m - i\tau_c\left(\omega + \overline{u}_T k\right)\right]}. \tag{33}$$

In this case, the relative contribution of ψ_T and ψ_B to P' depends on the magnitude of ω relative to $\overline{u}_T k$. For $\overline{u}_T k \gg \omega$, the polarization relation for P' simplifies to

$$P' \sim \frac{i\overline{M}_q \overline{u}_T k k_d^2}{f_0\left[m - i\tau_c\left(\omega + \overline{u}_T k\right)\right]}\psi'_B, \tag{34}$$

which indicates that P' is governed by the barotropic mode, which governs the advection of mean midtropospheric temperature [Eq. (13c)]. This approximation is accurate in regions where $\overline{u}_T > 10\,\mathrm{m\,s^{-1}}$ and for zonal wavenumbers greater than 10. These conditions are reasonable for both MLPSs and AEWs. If we replace P' by q'_3 in Eq. (34) we obtain the following approximate proportionality:

$$q'_3 \propto \tau_c \psi'_B, \tag{35}$$

which illustrates that the moisture anomalies increase in amplitude as τ_c is increased. When $\tau_c = 0$, no moisture anomalies exist but P' can be nonzero, as shown by Eq. (32b). Thus, interactions between the large-scale circulation and moisture require $\tau_c > 0$.

The phase relation between ψ'_B and ψ'_T will provide key insights into the interpretation of the main instabilities in this study. We can obtain the phase angle between the two fields by rearranging the terms in Eq. (32a) and decomposing ω into its real and imaginary parts $\omega = \omega_r + i\omega_i$, which yields the following expression:

$$\tan\left(\alpha_\psi - \pi\right) = \frac{\omega_i k}{\beta + \omega_r k}\mathrm{sgn}\left(\overline{u}_T\right), \tag{36}$$

where α_ψ is defined so that it is zero in regions of easterly shear in which $\beta + \omega_r k$. The sign function (sgn) takes into account the fact that the polarization relation in Eq. (32a) is dependent on the sign of $\overline{u}_T$. A schematic showing how the phasing between ψ_T and ψ_B vary as a function of α_ψ is shown in Fig. 3a.

Equation (36) along with Fig. 3a reveal that the larger ω_i is relative to ω_r, the more tilted the vertical structure of the wave is. This result is clearest when considering the case of $\beta = 0$. In this simplified case the angle is just the ratio between ω_r and ω_i. In the Eady (1949) model of baroclinic instability, $\omega_r = 0$ when $\omega_i > 0$, which results in $\alpha_\psi = -90°$. Neutrally stable waves are vertically stacked and tend to be either top-heavy or bottom-heavy, as discussed by Wang and Xie (1996).

The relationship between P' and ψ'_B will also elucidate the processes that lead to instability in the moist waves analyzed here. We can obtain an approximate relationship following AM18, rearranging the terms in Eq. (32b) and assuming $m \gg \tau_c(\omega + \overline{u}_T k)$. The resulting phase relationship takes the following form:

$$\tan\alpha_P \simeq -\frac{m}{\tau_c k\left(c_p + \overline{u}_T\right)}\mathrm{sgn}\left(\overline{u}_T\right), \tag{37}$$

where $c_p = \omega_r/k$ is the phase speed of the wave relative to the barotropic flow, recalling that $\omega_r = \omega_r^* - \overline{u}_B$. Equation (37) is analogous to Eq. (27) in AM18 with the addition of a $\overline{u}_T$ term and that the phasing is specifically with respect to ψ'_B. Figure 3b shows the phasing between P' and ψ'_B. Similarly to AM18, $\alpha_P = 90°$ if $\tau_c = 0$. When $\tau_c > 0$, a component of P' will be in phase with ψ'_T, which leads to growth through moisture–vortex instability or decay, depending on the value of α_P (Fig. 3b).

4. Solutions for $\tau_c = 0$

The dispersion relation in Eq. (31a) includes a multitude of terms that involve various processes. As a result, it may be daunting to elucidate the processes that lead to wave propagation and growth without first considering some simplifications. The first simplification worth discussing are the

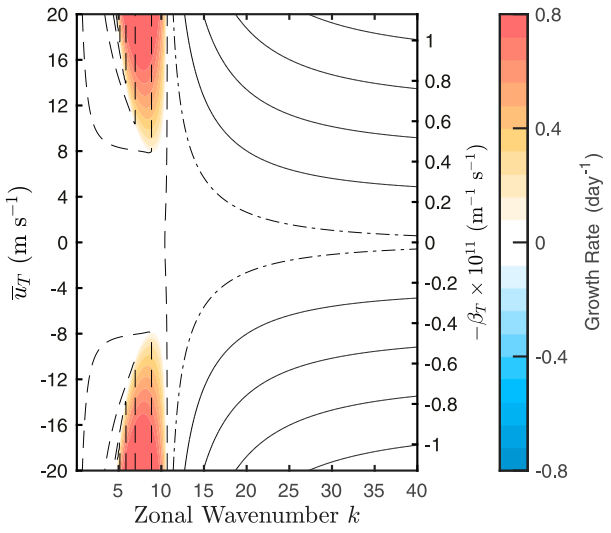

FIG. 4. Growth rate (shading) and phase speed (contours) as a function of zonal wavenumber and thermal wind $\overline{u}_T$ for the growing wave solution when $\tau_c = 0$, $\beta_q = 0$, and $m = 0.2$. The contour interval is 2.5 m s^{-1}. The dot–dashed line depicts a phase speed of zero, while dashed lines depict negative (westward) phase speeds. The left ordinate shows $\overline{u}_T$ and the right ordinate shows β_T.

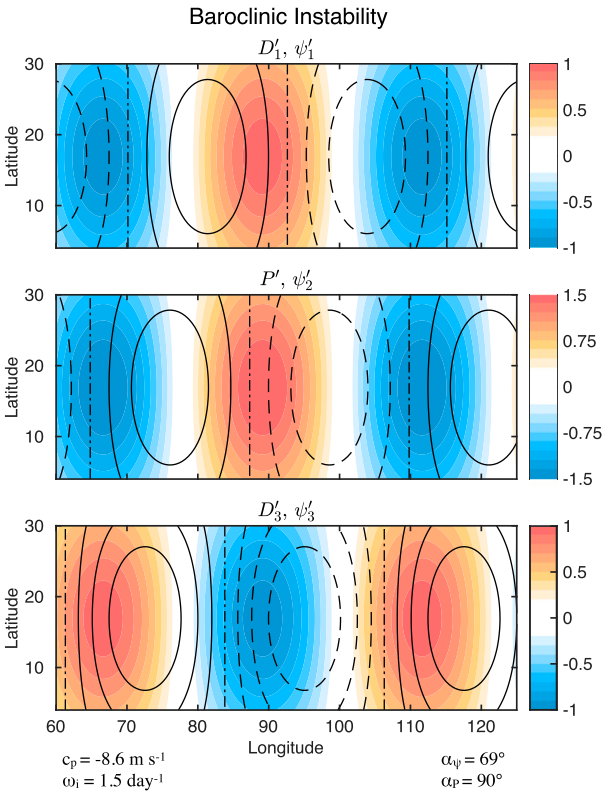

FIG. 5. Horizontal map of a zonal wavenumber-8 wave that grows from baroclinic instability, where $\overline{u}_T = -20$ m s^{-1}, $\beta_q = 0$, $\tau_c = 0$, and $m = 0.2$. (top) Upper-tropospheric streamfunction ψ_1' and divergence D_1'. (middle) Midtropospheric streamfunction ψ_2' and precipitation anomalies P'. (bottom) Lower-tropospheric streamfunction ψ_3' and divergence D_3'. The contours and shading in both panels are based on an initial anomaly of ψ_T' (ψ_{T0}) of 5×10^5 m^2 s^{-1}. The contour interval is 2×10^5 m^2 s^{-1}. While the meridional structure is not discussed in this study, it is chosen here so that it is much longer than the horizontal structure, effectively making it negligible.

well-documented solutions that arise in an atmosphere where precipitation is diagnosed from large-scale forcing ($\tau_c = 0$). In such a case, Eq. (31a) simplifies to

$$m\mathfrak{B}_d + (1-m)\mathfrak{B}_m = 0. \tag{38}$$

The dispersion relation that arises from this case will be denoted with a subscript 0 (i.e., ω_0). The full solution to Eq. (38) takes the form

$$\omega_0 = -\frac{\beta(2mk^2 + k_d^2) + \beta_q k^2(1-m)}{2k(mk^2 + k_d^2)} \pm \delta, \tag{39a}$$

where

$$\delta = \left\{ \frac{[\beta k_d^2 - \beta_q k^2(1-m)]^2}{4k^2(mk^2 + k_d^2)^2} - \frac{\overline{u}_T^2 k^2(k_d^2 - mk^2) - \overline{u}_T k^2 \beta_q (1-m)}{mk^2 + k_d^2} \right\}^{1/2}. \tag{39b}$$

The dispersion contains two solutions: a growing mode and a damped mode. The phase speed and growth rate of the growing mode is shown in Fig. 4 for $\beta_q = 0$ and $m = 0.2$. Propagation of the wave is westward at the largest scales, although it becomes eastward for zonal wavenumbers greater than 10 when $|\overline{u}_T| > 8$ m s^{-1}. No difference in propagation and growth is seen between easterly $\overline{u}_T$ and westerly $\overline{u}_T$. The damped solution mirrors the growing one and is not shown.

The terms within the square root in δ are comprised of a combination of terms that are weighted by m or $1 - m$. The former terms correspond to the processes that lead to dry baroclinic instability while the latter lead to moist baroclinic instability [see section b(2) of the appendix]. When $0 < m < 1$ growth occurs due to a combination of dry and moist baroclinic instabilities. Waves that grow this way are often referred to as diabatic Rossby waves (Parker and Thorpe 1995). We will refer to this instability as baroclinic instability without any distinction, while the growth when $m = 1$ and $m = 0$ will be referred to as dry and moist baroclinic instabilities, respectively.

Relative to dry baroclinic instability alone, growth between $m = 0$ and $m = 1$ exhibits a larger amplitude due to the contribution from moist processes. This larger amplitude was noted in the diabatic Rossby waves examined by de Vries et al. (2010), and by the balanced moist waves examined by Wetzel et al. (2017). In the case of $\beta = 0$ and $\beta_q = 0$ we find that baroclinic instability occurs when $k < k_d m^{-1/2}$. This result is similar to the dry case [see section b(1) of the appendix], except k is scaled by $m^{-1/2}$, which indicates that the cutoff for instability occurs at smaller scales (larger k).

Waves that grow from baroclinic instability in easterly shear ($\overline{u}_T < 0$) exhibit an eastward tilt with height (Fig. 5). The strong

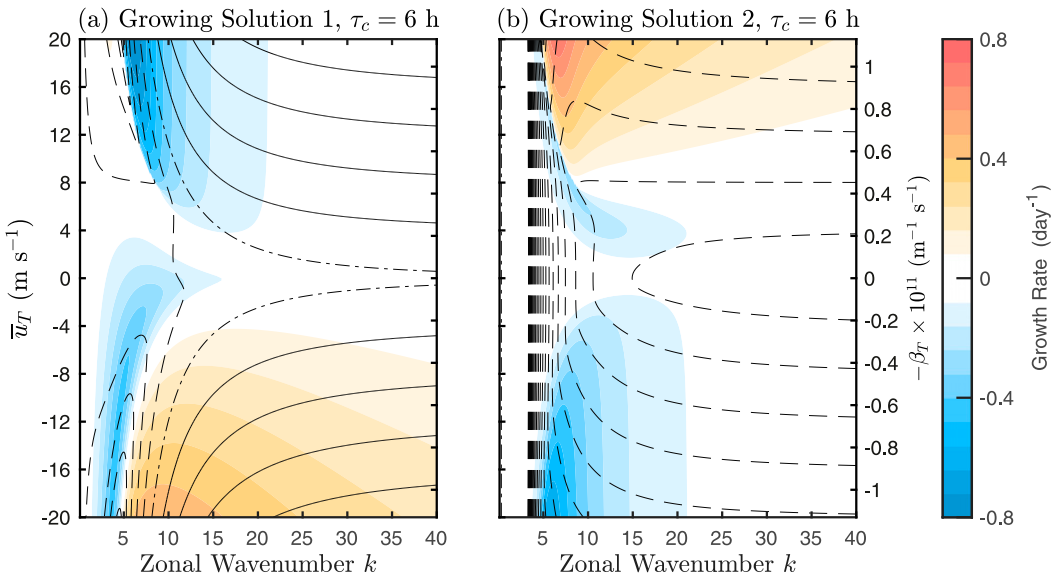

FIG. 6. As in Fig. 4, but showing the two growing wave solutions that arise when $\tau_c = 6$ h.

tilt is the result of the large growth rate relative to the propagation speed, as indicated by Eq. (36).

5. Solutions for $\tau_c > 0$

So far, we have discussed the behavior of wave solutions when convection instantaneously responds to large-scale forcing, $\tau_c = 0$. In this section we will investigate how this behavior changes when moisture is prognostic, i.e., $\tau_c > 0$.

When $\tau_c > 0$, Eq. (31a) yields three wave solutions: one that grows when $\overline{u}_T > 0$, one that grows when $\overline{u}_T < 0$, and a damped mode. The growth rate and phase speeds for the two growing modes is shown in Fig. 6. While the solutions for $\tau_c = 0$ exhibit symmetry with respect to the direction of $\overline{u}_T$ when $\beta_q = 0$, a nonzero τ_c breaks this symmetry.[2] For $\tau_c = 6$ h, growth begins near zonal wavenumber 6 for both easterly and westerly $\overline{u}_T$. This is the same zonal wavenumber where baroclinic instability begins to be observed in Fig. 4. However, when $\tau_c = 6$ h growth is also observed for larger wavenumbers than those seen in Fig. 4. Additionally, while baroclinic instability is seen only when $\overline{u}_T$ has a magnitude of 10 m s^{-1} or greater, growth in easterly shear can be seen for $\overline{u}_T$ values of magnitude greater than 4 m s^{-1}. In westerly shear, however, damping is seen between 4 and 10 m s^{-1}. The largest growth rates when $\tau_c = 6$ h are smaller in amplitude than the largest growth rates when $\tau_c = 0$.

The growth rates in Fig. 6 are distinct from those Fig. 4, suggesting that these waves may not be growing from baroclinic instability. Instead, they may be growing from an instability that requires a prognostic moisture equation ($\tau_c > 0$). We can elucidate this instability by obtaining an approximate solution to Eq. (31a). We will assume that, to leading order, the $\tau_c = 0$ solutions describe the behavior of the wave. With these assumptions we can expand Eq. (31a) into a perturbation series, centered on the $\tau_c = 0$ solutions and truncating on the second term:

$$\omega \simeq \omega_0 + \varepsilon\omega_1 . \tag{40}$$

In Eq. (40), ω_0 is the dispersion relation for Eq. (38), ε is a small nondimensional parameter and ω_1 is the second-order wave solution. Nondimensionalizing Eq. (31a) reveals that $\varepsilon = \tau_c f_0$ (not shown). The approximate solution is robust as long as $\tau_c f_0 \ll m$. For $m \simeq 0.2$ and $f_0 = 4 \times 10^{-5}$ s^{-1}, τ_c would need to be on the order of 8 min for the perturbation expansion to be accurate. We will use a value of 0.1 h (6 min) for our approximate solution. While we recognize that τ_c is actually on the order of hours (Betts and Miller 1986; Bretherton et al. 2004; Ahmed et al. 2020), this approximate solution is still sufficiently insightful to be worth discussing.

Applying the perturbation series expansion in Eq. (40) to Eq. (31a) leads to the following approximate dispersion relation:

$$\omega \simeq \omega_0 + i\tau_c(\omega_0 + \overline{u}_T k)\omega_0 \mathfrak{M} \tag{41a}$$

where

$$\mathfrak{M} = \frac{\mathfrak{B}_d}{\mathfrak{R}} \tag{41b}$$

accounts for interactions between moisture and vorticity, and will be referred to as the moisture–vortex interaction term. The denominator term $\mathfrak{R}$ is defined as

$$\mathfrak{R} = \omega_0^2 k\left(mk^2 + k_d^2\right) - \beta k\left[m\beta + (1-m)\beta_q\right] - \overline{u}_T^2 k^3\left(k_d^2 - mk^2\right) + (1-m)\beta_q \overline{u}_T k^3 . \tag{41c}$$

[2] The symmetry between easterly and westerly $\overline{u}_T$ is specific to the two-layer model used in this study, in which the depths of the two layers are equal and $\overline{u}_T$ does not vary in space and time. If the two layers have different pressure depths or if a horizontal gradient in $\overline{u}_T$ is included, a symmetry between westerly and easterly $\overline{u}_T$ will not be seen even when $\tau_c = 0$.

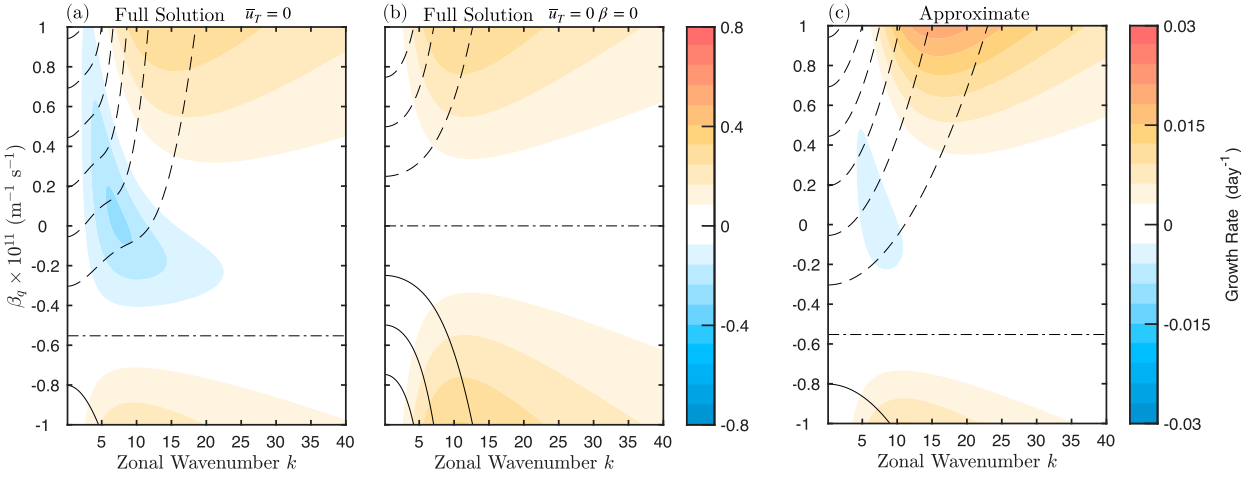

FIG. 7. (a) Growth rate (shading) and phase speed (contours) obtained from Eq. (31a) as a function of varying β_q and assuming $\overline{u}_T = 0$. (b) As in (a), but assuming $\beta = 0$. For (a) and (b) $\tau_c = 6$ h and $m = 0.2$. (c) As in (a), but showing the approximate solution obtained from Eq. (41a) and $\tau_c = 6$ min. Units on the ordinate are multiplied by 10^{11}. Note that the scale in the color bar of (c) is reduced by a factor of 26 compared to (a) and (b), largely as a result of the smallness of τ_c in the approximate solution.

In a dry atmosphere $\mathfrak{B}_d = 0$ and hence $\mathfrak{M} = 0$. The moisture–vortex interaction term $\mathfrak{M}$ can also be written in terms of moist processes by using Eq. (38) and replacing $\mathfrak{B}_d$ with $\mathfrak{B}_m$:

$$\mathfrak{M} = -\frac{(1-m)\mathfrak{B}_m}{m\mathfrak{R}}. \tag{42}$$

Equation (42) shows that moisture–vortex interactions amplify with decreasing m, consistent with the growth rates obtained by AM18 (see also supplementary material). While $\mathfrak{B}_m \to 0$ as $m \to 0$, it does so at a slower pace than $(1-m)/m$ increases (not shown). The denominator term $\mathfrak{R}$ also tends to decrease with decreasing m, compensating for the decrease in $\mathfrak{B}_m$ as m decreases. Thus, interactions between perturbations in moisture and vorticity become more important as the lower troposphere becomes more humid.

The real component of the second term in Eq. (41a) contributes negligibly to the propagation of the wave, as seen when comparing the contours of Figs. 4 and 6a. Because of this, we can simplify Eq. (41a) to elucidate the processes that arise when $\tau_c > 0$ by decomposing ω_0 and $\mathfrak{M}$ into their real and imaginary components (subscripts r and i, respectively):

$$\omega_0 = c_p k + i\delta_i, \tag{43a}$$

$$\mathfrak{M} = \mathfrak{M}_r + i\mathfrak{M}_i, \tag{43b}$$

where δ_i is the imaginary component of δ. With this decomposition, we can simplify Eq. (41a) to

$$\omega \simeq c_p k + i(\mathrm{MVI} + \mathrm{BCI} + \mathrm{BMI}), \tag{44a}$$

where we have defined three different processes that contribute to wave growth or decay. The first imaginary term in Eq. (44a) is

$$\mathrm{MVI} = \tau_c k^2 c_p \left(c_p + \overline{u}_T\right)\mathfrak{M}_r, \tag{44b}$$

which we will refer to as the moisture–vortex instability term due to its similarity to the instability described by AM18. The second term,

$$\mathrm{BCI} = \delta_i\left(1 - \tau_c \mathfrak{M}_r \delta_i\right), \tag{44c}$$

is the growth rate from baroclinic instability. The first term in Eq. (44c) is the baroclinic instability term from Eq. (39), while the second term is a modulation from the addition of prognostic moisture. The third term is written as

$$\mathrm{BMI} = -\tau_c k \delta_i \left(2c_p + \overline{u}_T\right)\mathfrak{M}_i, \tag{44d}$$

which will be referred to as the baroclinic moisture–vortex interaction term since it contains contributions from baroclinic instability δ_i and the parenthesis term is reminiscent to the MVI term.

The three processes defined in Eq. (44a) contain information about how moist waves can grow. We will discuss MVI first since it is a process that occurs independently from baroclinic instability. We will then analyze how the three terms add up to create growth or decay in moist waves.

a. β_q-induced moisture–vortex instability

The simplest case of moisture–vortex instability can be obtained when $\beta_q \neq 0$ and $\overline{u}_T = 0$. In such a case the BCI and BMI terms in Eq. (44a) are zero but MVI can be nonzero. Figures 7a and 7c show the phase speed and growth rate obtained with Eqs. (31a) and (41a), respectively. While the approximate solution from Eq. (41a) exhibits much smaller growth rates than the solution from Eq. (31a) due to the much smaller value of τ_c, it does qualitatively capture the same pattern. The largest growth is seen when $\beta_q > 0$ near zonal wavenumber 15. Damping at the largest scales is also seen. It is worth noting that the wavenumber–β_q distribution of growth rates for β_q-induced moisture–vortex instability is similar to the wavenumber–β_T distribution seen for $\overline{u}_T < 0$ ($\beta_T > 0$) in

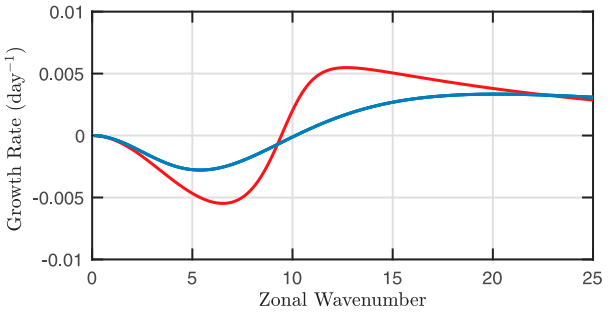

FIG. 8. Growth rate as obtained from Eq. (44a) for $\overline{u}_T$-induced moisture–vortex instability (red) and for β_q-induced moisture–vortex instability (blue). For the red line $u_T = -5\,\mathrm{m\,s^{-1}}$ ($\beta_T = 0.3 \times 10^{-11}\,\mathrm{m^{-1}\,s^{-1}}$) and $\beta_q = 0$. For the blue line $u_T = 0$ and $\beta_q = 0.3 \times 10^{-11}\,\mathrm{m^{-1}\,s^{-1}}$. For both lines $\tau_c = 6$ min and $m = 0.2$.

Fig. 6a, hinting that the growth rates are the result of similar instabilities. Growth rates when $\beta_q < 0$, in contrast, are weaker and are largest near zonal wavenumber 10. No damping is seen at the largest scales.

One of the striking features of Fig. 7a is the asymmetry between negative and positive values of β_q. This asymmetry is the result of the β effect. When $\beta = 0$ (Fig. 7b), no asymmetry is seen between positive and negative values of β_q. From inspection of Eq. (44b), we can see that the contribution of β to the asymmetry in Fig. 7a comes from $\mathfrak{M}_r$.

b. $\overline{u}_T$-induced moisture–vortex instability

The growth rates shown in Fig. 6 reveal growth beyond the region where baroclinic instability is observed in Fig. 4. Equation (44a) indicates that growth in these regions may be due to moisture–vortex instability induced by a temperature gradient (β_T). This hypothesis is based on the fact that MVI is the only growth term in Eq. (44a) that does not require baroclinic instability (positive δ_i).

The red line in Fig. 8 shows the contribution of Eq. (44b) to the growth of wave when $\beta_q = 0$ and $\overline{u}_T = -5\,\mathrm{m\,s^{-1}}$ ($\beta_T = 0.3 \times 10^{-11}\,\mathrm{m^{-1}\,s^{-1}}$). This value of $\overline{u}_T$ is chosen since it can be seen from comparing Figs. 4 and 6 that baroclinic instability does not occur in this region ($\delta_i = 0$). Comparison with β_q-induced moisture vortex reveals many similarities. Both cases exhibit damping at the largest scales and growth that is largest at the synoptic scale. However, some differences are also observed. The growth rate associated with $\overline{u}_T$ peaks at larger amplitudes than those associated with β_q alone. Additionally, the largest growth rate for the $\overline{u}_T$-only instability is largest at zonal wavenumber 12, whereas it is a maximum at zonal wavenumber 20 for the β_q-only moisture vortex instability. Nonetheless, the broad similarities between the two growth rates and the fact that both arise from the MVI term leads us to conclude that the $\overline{u}_T$-based instability examined in Fig. 8 is a type of moisture–vortex instability.

In spite of the similar growth rates, the vertical structure of the waves that grow due to these two types of moisture–vortex instabilities are different. Figure 9b shows that the β_q-based moisture–vortex instability has no signature in the midtroposphere, i.e., $\psi'_B = 0$. In comparison, the $\overline{u}_T$-only instability exhibits a structure that is comprised of nearly equal parts barotropic and baroclinic structures (Fig. 9a). The baroclinic and barotropic structures are nearly out of phase, so that the resulting wave structure is bottom-heavy ($\alpha_\psi \simeq 0$). As a result, $\overline{u}_T$-only moisture–vortex instability exhibits a wave structure that is distinct from baroclinic instability, in which the wave structure tilts with height against the shear (Fig. 5).

c. Gross PV perspective on moisture–vortex instability

We can further understand the moisture–vortex instability mechanism by rearranging the terms in Eq. (28) in such a way that it becomes an equation that describes the evolution of ψ'_T. The rearrangement yields the following equation:

$$\frac{\overline{D}_h}{Dt}\left[m\nabla_h^2\psi'_T + (1-2m)k_d^2\psi'_T\right] = \mathrm{Pr} + \mathrm{Gr}, \tag{45a}$$

where

$$\mathrm{Pr} = (1-m)\left[-v'_T\beta_q - v'_B\beta_m\right] - m\left[-v'_T\beta + v'_B\beta_T - \overline{u}_T\frac{\partial\zeta'_B}{\partial x}\right], \tag{45b}$$

$$\mathrm{Gr} = -\left(\frac{\partial}{\partial t} - \overline{u}_T\frac{\partial}{\partial x}\right)\frac{f_0\tau_c}{\overline{M}_q}P', \tag{45c}$$

are the terms that describe the propagation and growth of ψ'_T, respectively. The propagation term Pr contains the same terms that we saw in the case of baroclinic instability. However, in baroclinic instability these terms could also cause instability and growth. In moisture–vortex instability, growth depends on terms that have τ_c, i.e., water vapor (recall that $q'_3 = \tau_c P'$). The negative sign has to do with the definition of ψ_T, which is positive for upper-tropospheric cyclones and hence is negative for lower-tropospheric cyclones. Thus, instability occurs when a positive moisture tendency is spatially collocated with a cyclonic vorticity tendency. This growth can be enhanced or damped by the baroclinic component of the lower-tropospheric flow, which has the opposite polarity of $\overline{u}_T$ (recall that $\overline{u}_3 = \overline{u}_B - \overline{u}_T$).

Figure 10 shows how $\overline{u}_T$ can either enhance or suppress moisture–vortex instability when $\overline{u}_B = 0$, i.e., $\overline{u}_3 = -\overline{u}_T$. For a westward-propagating disturbance, westerly shear ($\overline{u}_T > 0$) advects the lower-tropospheric moisture away from the vortex. This advection increases α_P and thus weakening or even preventing moisture–vortex instability. In the case of easterly shear ($\overline{u}_T < 0$), the lower-tropospheric westerlies advect the anomalous rainfall toward the center of low pressure, reducing α_P. To first order, Gr is represented by the denominator terms in α_P. Thus, moisture–vortex instability occurs as long as $\alpha_P < 90°$.

In observations it is likely that $-\overline{u}_B$ is nonzero and so $\overline{u}_3$ may not correspond to $-\overline{u}_T$. However, the relationship in Fig. 10 is still applicable if the barotropic component of the zonal wind is removed since it does not play a role in determining α_P (not shown).

6. Does baroclinic instability weaken when $\tau_c > 0$?

So far, we have shown that when $\tau_c > 0$ moisture–vortex instability arises as a mechanism for wave growth. This instability is

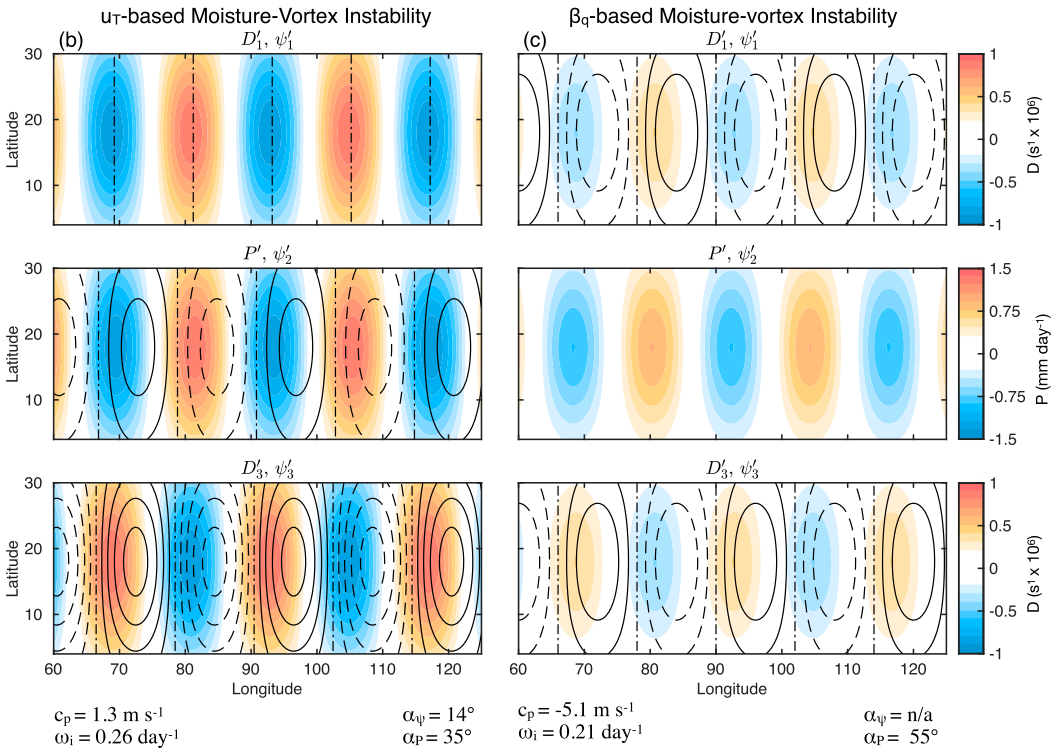

FIG. 9. As in Fig. 5, but showing a zonal wavenumber-15 wave that grows from (a) $\overline{u}_T$-based moisture–vortex instability, where $\overline{u}_T = -7\,\mathrm{m\,s^{-1}}$, $\beta_q = 0$, and (b) β_q-based moisture–vortex instability, where $\overline{u}_T = 0$ and $\beta_q = 0.4\,\mathrm{m^{-1}\,s^{-1}}$. In both panels $m = 0.2$ and $\tau_c = 6\,\mathrm{h}$.

summarized in the MVI term in Eq. (44a). However, we have not discussed how baroclinic instability is modified by prognostic moisture, and how moisture–vortex and baroclinic instabilities could interact with one another.

Figure 11 shows the contribution of MVI, BCI and BMI to the growth of a wave. BMI and BCI are added since both terms require δ_i to be nonzero. It is clear that baroclinic instability (δ_i) and moisture–vortex instability MVI occur separately and

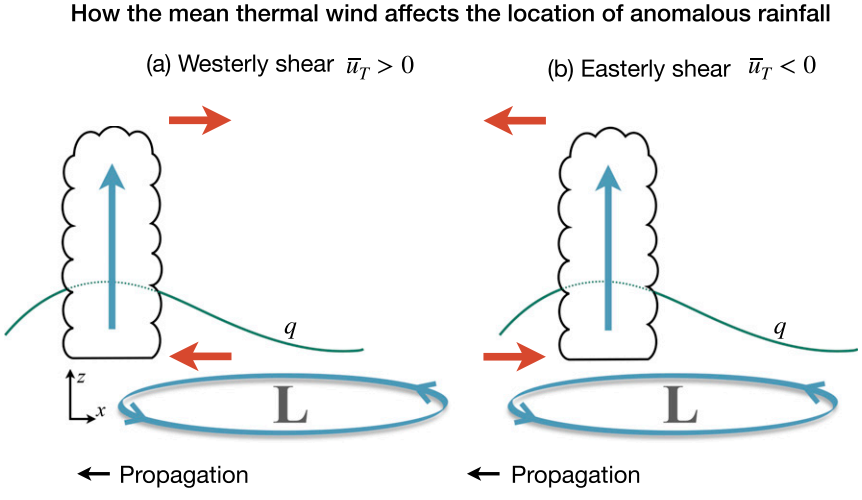

FIG. 10. Schematic describing how the mean thermal wind $\overline{u}_T$ (red arrows) affects the phasing between anomalous lower-tropospheric circulation and anomalous rainfall. A westerly ($\overline{u}_T > 0$) thermal wind corresponds to mean lower-tropospheric easterlies when $\overline{u}_B = 0$. The lower-tropospheric moisture q_3 is shown as a blue–green line, and the vertical velocity associated with convection (ω_Q) is shown as the teal vertical arrow.

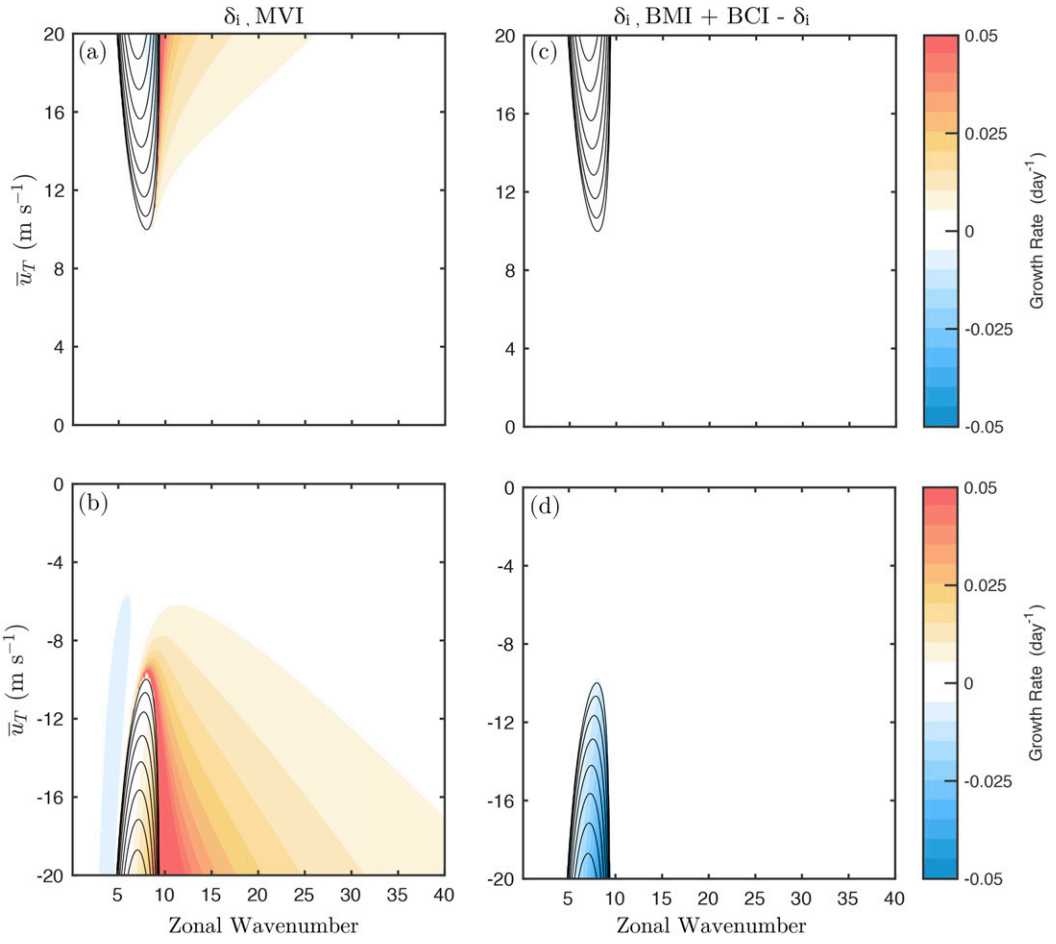

FIG. 11. Growth rate contribution from (a),(b) MVI and (c),(d) the modulation of baroclinic instability when $\tau_c > 0$, which is written as BCI + BMI − δ_i for the growing modes obtained from Eq. (44a). (a),(b) The section in Fig. 6a where $\overline{u}_T > 0$. (c),(d) The section in Fig. 6a where $\overline{u}_T < 0$. In all panels the contribution of baroclinic instability δ_i to growth is shown as contours. The contour interval is 0.2 day^{-1}.

barely overlap when considering the approximate relation in Eq. (44a).

A comparison of Figs. 11a and 11b reveals that moisture–vortex instability is stronger when $\overline{u}_T < 0$ than when $\overline{u}_T > 0$. This difference in amplitude of MVI is related to β, which impacts the propagation of the moist wave in an analogous way to what was shown when considering β_q-only instability. When $\beta = 0$, the MVI term is symmetric with respect to the sign of $\overline{u}_T$ (see supplementary material).

When considering the modulation of baroclinic instability when $\tau_c > 0$ (Figs. 11c,d), we see that baroclinic instability is weakened when $\overline{u}_T < 0$. In contrast, there is little modulation of baroclinic instability when $\overline{u}_T > 0$. This difference between $\overline{u}_T < 0$ and $\overline{u}_T > 0$ is due to the BMI term. Because c_p is westward at the wavenumbers that correspond to baroclinic instability (see Fig. 4), it follows that BMI is larger in magnitude for $\overline{u}_T < 0$ because the two contributions add up. For $\overline{u}_T > 0$, c_p and $\overline{u}_T$ cancel one another and BMI is small.

It is worth noting that the MVI term [Eq. (44b)] and the terms that contribute to the weakening of baroclinic instability [Eqs. (44c) and (44d)] scale with τ_c. Thus, moisture–vortex instability strengthens and baroclinic instability weakens as τ_c increases. We can see this change even when considering the full solutions from Eq. (31a) for different values of τ_c (Fig. 12). As τ_c increases, the growth rate in the regions that are outside the region of baroclinic instability become larger in amplitude. In turn, growth rates in the region of baroclinic instability weaken. This change is seen for both easterly and westerly $\overline{u}_T$, but it is stronger for easterly $\overline{u}_T$.

The mechanism in which moisture–vortex instability amplifies at the expense of baroclinic instability can be understood by examining how α_ψ and α_P change with increasing τ_c (Fig. 13). When τ_c is very small, α_ψ is near zero everywhere except for the region where baroclinic instability is seen, where the angle quickly increases to ~90°. The angle between P' and ψ'_T is close to ~90° indicating that precipitation is in quadrature with ψ'_T for nearly all zonal wavenumbers and values of $\overline{u}_T$. As τ_c increases, α_P decreases, as expected from Eq. (37). It decreases the fastest in regions of $\overline{u}_T < 0$ where baroclinic instability is observed. The phase angle α_ψ also decreases rapidly in

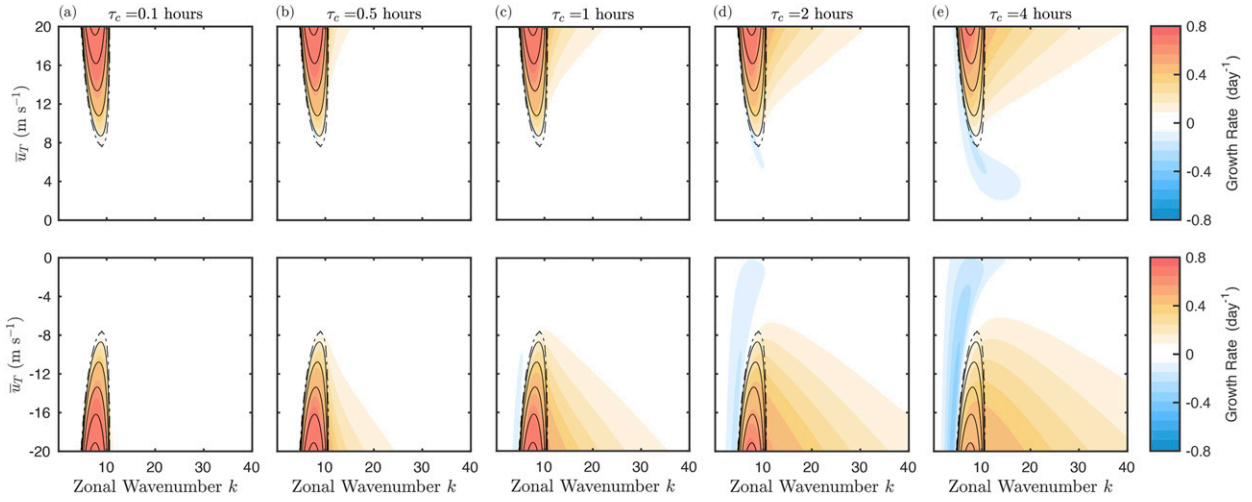

FIG. 12. Growth rates for the unstable mode obtained from Eq. (31a) for $\beta_q = 0$, $m = 0$, and (top) $\overline{u}_T > 0$ and (bottom) $\overline{u}_T < 0$ for τ_c values of (a) 0.1, (b) 0.5, (c) 1, (d) 2, and (e) 4 h. Growth from baroclinic instability δ_i is shown as contours for each panel. The panels are arranged as in Fig. 11. The zeroth contour is shown as a dot–dashed line.

this region. In contrast, both α_P and α_ψ decrease more slowly in the westerly shear regions where baroclinic instability is observed.

We can use Figs. 10 and 13 to explain why baroclinic instability weakens more rapidly when $\overline{u}_T < 0$. The rapidly decreasing α_P favors moisture–vortex instability, since more vortex stretching from convection occurs near the center of a vortex. Furthermore, the reduction of α_ψ indicates weaker tilt with height in the moist wave, which is less favorable for the generation of available potential energy associated with baro clinic instability (Eady 1949). The reduction in both α_P and α_ψ indicate that the structure of the moist wave shifts toward a structure that is more consistent with moisture vortex instability, i.e., precipitation shifted toward the surface low and small α_ψ, which favors a vertically stacked, bottom-heavy vertical structure.

We can confirm the results from Fig. 13 by examining the horizontal structure of the growing waves under westerly and easterly $\overline{u}_T$ (Fig. 14). When $\tau_c = 6$ h, the growing wave under westerly $\overline{u}_T$ still exhibits a structure that is reminiscent to baroclinic instability. We observe the westward tilt in height of ψ', and the large-scale adiabatic lifting (ω'_a) is approximately in phase with the convectively driven ascent (ω'_Q). In contrast, the structure of the growing wave under easterly $\overline{u}_T$ exhibits a structure more reminiscent to moisture–vortex instability, and consistent with the structure of observed and simulated MLPSs (Chen et al. 2005; Adames and Ming 2018b; Clark et al. 2020; Murthy and Boos 2020). Precipitation is shifted toward the

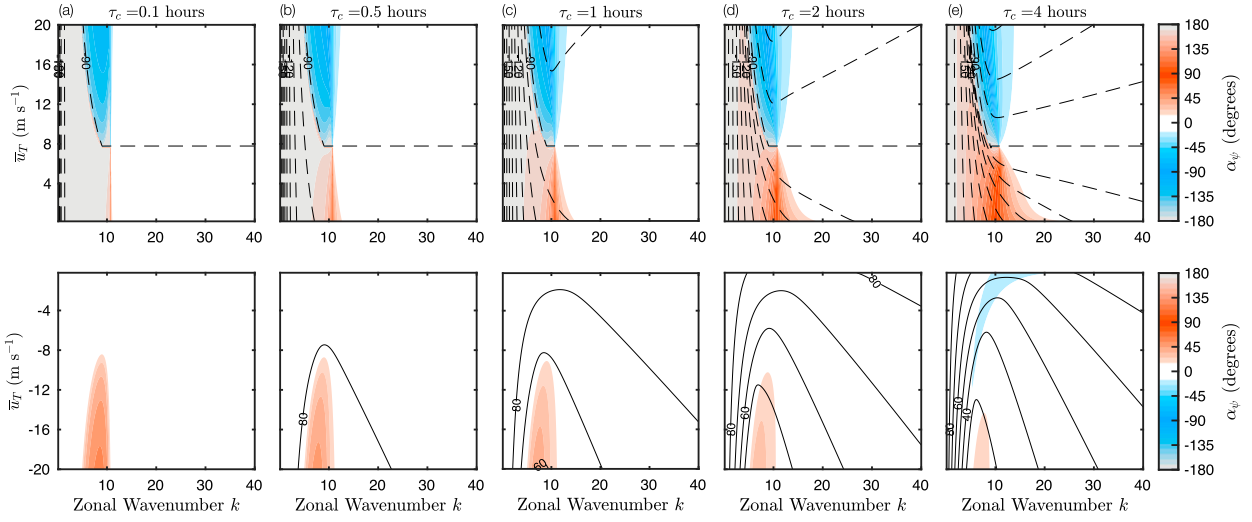

FIG. 13. As in Fig. 12, but showing α_ψ as shading and α_P as contours defined as in Fig. 3. The angle α_ψ is defined as a tilt against the shear, with increasing α_ψ meaning increased tilt against the shear. The angle α_P is defined as a westward shift of P' with respect to $-\psi'_T$.

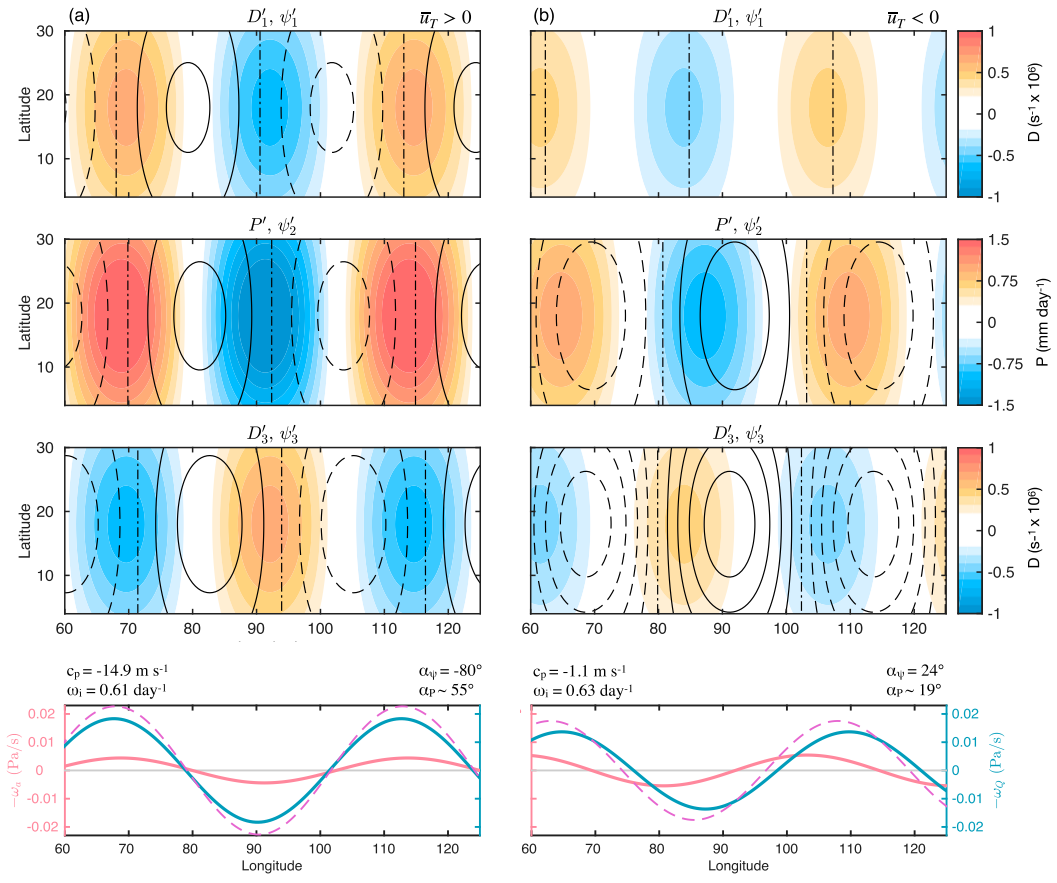

FIG. 14. (top three rows) As in Fig. 5, but showing the growing zonal wavenumber-8 solutions of Eq. (31a) for (a) $\overline{u}_T = 20\,\mathrm{m\,s^{-1}}$ and (b) $\overline{u}_T = -20\,\mathrm{m\,s^{-1}}$. For both solutions $\tau_c = 6$ h, $m = 0.2$, and $\beta_q = 0$. (bottom) Adiabatic ω_a (pink), diabatic (teal), and total (purple dashed) vertical velocity anomaly averaged over 10°–25°N.

vortex and very little wave signature is seen in the upper troposphere. Additionally, ω_a' is shifted to the west of ω_Q'. Perhaps the only signature of baroclinic instability seen in this case is the weak eastward tilt with height seen in ψ'. This bottom-heavy structure is maintained for growing modes even when β_q is nonzero (see supplementary material).

7. Synthesis and discussion

In this study, we analyze a linear two-layer QG model with prognostic moisture. The moisture is coupled to precipitation through a simplified Betts–Miller-like scheme. We investigate how moisture impacts the instability and scale selection of waves that propagate in the presence of a thermal wind $\overline{u}_T$. The wave solutions obtained in this study can be described as moist Rossby waves that can grow from two instabilities, whose characteristics are summarized in Table 3:

- Baroclinic instability: Two counterpropagating waves in the presence of $\overline{u}_T$ become phase locked. The waves amplify one another via generation of available potential energy that occurs due to upward motion induced by temperature and vorticity advection, or through vortex stretching from convection induced by the aforementioned processes. The salient feature of this instability is the tilt with height of PV and associated wind fields (Fig. 1a). Large-scale adiabatic lifting (ω_a') and convectively driven (ω_Q') ascent are in phase.
- Moisture–vortex instability: Moistening of the lower troposphere by horizontal moisture and temperature advection induce a buildup of moisture, which enhances precipitation. The moisture anomalies exhibit an in-phase component with the vortex, which grows through vortex stretching (Fig. 1b). Unlike baroclinic instability, waves that grow through moisture–vortex instability do not exhibit significant tilts with height. Unlike baroclinic instability, ω_a' is shifted to the west of ω_Q'.

Both baroclinic and moisture–vortex instability share some similarities. Both instabilities are enhanced by a lower NGMS (m) and when the temperature and moisture gradients (β_T and

TABLE 3. Comparison of the two main instabilities discussed in this study.

Instability	$\lvert\alpha_\psi\rvert$	$\lvert\alpha_p\rvert$	Preferred $\overline{u}_T$
Baroclinic	~90°	90°	Westerly
Moisture–vortex	~0°	<90°	Easterly

β_q) are in the same direction (see supplementary material). However, both instabilities also exhibit distinct differences. Baroclinic instability is strongest when precipitation responds instantaneously to convection ($\tau_c = 0$) while moisture–vortex instability becomes stronger with increasing τ_c.[3] Furthermore, when $\tau_c > 0$ the β effect causes moisture–vortex instability to be stronger over easterly shear than over westerly shear. The opposite is true for baroclinic instability. Our study indicates that, in regions of high humidity, moisture–vortex instability may be the preferred instability in regions of easterly shear while baroclinic instability is dominant in regions of westerly shear.

Our results may shed some insights onto the mechanism of growth of several tropical motion systems.

a. *Monsoon low pressure systems*

The results of this study may be most applicable to MLPSs. As discussed by Cohen and Boos (2016), the horizontal structure of these systems does not exhibit the vertical tilts characteristic of baroclinic instability. Studies by Chen et al. (2005), Adames and Ming (2018b) and Clark et al. (2020) show that these systems exhibit a bottom-heavy, upright structures, consistent with Fig. 9a. Furthermore, large-scale adiabatic lifting in these systems is shifted to the west of the convectively driven ascent (Adames and Ming 2018b), consistent with the shifts shown in Fig. 14b. Thus, our results combined with observed structure of MLPSs suggest that these systems may grow from moisture–vortex instability.

Barotropic instability is also thought to play a role in the growth of MLPSs (Krishnamurti et al. 1976; Diaz and Boos 2019a,b). This study did not examine how moisture–vortex instability is affected in an environment with horizontal barotropic shear. However, we hypothesize that the moist barotropic instability mechanism proposed by Diaz and Boos (2019b) may be a combination of barotropic and moisture–vortex instabilities. Future work should examine possible interactions between these two instabilities.

It is worth pointing out that the phase speed in systems that grow from moisture–vortex instability under easterly shear exhibit weak propagation when the thermal wind is strong (Fig. 6). This propagation is weak even when considering β_q. However, both simulated and observed MLPSs exhibit some amount of west or northwest propagation (Boos et al. 2015; Clark et al. 2020). It is possible that MLPSs occur in weaker shear, and can thus propagate against the mean westerlies. Alternatively, a nonlinear mechanism such as beta drift may account for nearly all of the propagation of MLPSs, as posited by Boos et al. (2015).

b. *AEWs*

At first glance, our results may not seem directly applicable to AEWs. The African easterly jet exhibits a maximum near 600 hPa (Burpee 1972; Cook 1999). Such a jet cannot be described well with the two-layer model described here. However, it is possible that the preference of easterly shear to favor moisture–vortex instability may extend to shallower jets such as the African easterly jet. This hypothesis is supported by recent studies that analyzed the growth of AEWs. For example, Russell et al. (2020) argue that rotational stratiform instability may be the main mechanism that leads to growth in AEWs, playing a larger role than baroclinic and barotropic instability. Their proposed instability and the vertical structure of PV discussed by Russell and Aiyyer (2020) are reminiscent of moisture–vortex instability.

Another study by Núñez Ocasio et al. (2020) found that developing AEWs contain embedded mesoscale convective systems (MCSs) that propagate at the same speed as the wave. Nondeveloping AEWs, on the other hand, do not exhibit such phase locking. They posit that the phase locking between the developing AEWs and the MCSs could be regarded as observational evidence of moisture–vortex instability. The studies by Russell et al. (2020) and Núñez Ocasio et al. (2020) indicate that interactions between convection and PV in AEWs are essential to the growth of AEWs. However, more research is needed to understand the role of moisture–vortex instability in AEWs, and to determine if moisture–vortex instability is related to the rotational stratiform instability described in Russell et al. (2020).

c. *Tropical cyclogenesis*

The vertically stacked structure of the waves that grow due to moisture–vortex instability in the presence of $\overline{u}_T$ is reminiscent of the vertical structure of a tropical cyclone (Marks and Houze 1987; Moon et al. 2020). While the model described in this study may not necessarily apply to tropical cyclogenesis because of the underlying assumptions and linearity, it may nonetheless provide some indicators of the mechanisms in which cyclogenesis can occur under vertical wind shear. For example, it may be possible that cyclogenesis is enhanced by moisture–vortex instability, in which case it may be possible for tropical cyclones to preferentially occur in conditions of easterly shear.

d. *A baroclinic and moisture–vortex instability spectrum?*

So far, we have discussed baroclinic and moisture–vortex instability as nearly mutually exclusive phenomena. However, our results indicate that a spectrum between baroclinic and moisture–vortex instability may exist (see Fig. 14). Baroclinic and moisture–vortex instability comprise the ends of the spectrum. For the former both $|\alpha_\psi|$ and α_P are approximately 90°. For the latter $\alpha_\psi \simeq 0$ and $\alpha_P < 90°$ as indicated by Table 3. In reality, atmospheric phenomena could grow from a combination of both, as indicated by the spectrum values of α_ψ and α_P shown in Fig. 13. This spectrum would be analogous to the spectrum of barotropic and baroclinic instability (Krishnamurti et al. 1976; Thorncroft and Hoskins 1994), where the former occurs over strong horizontal shear and the latter over strong vertical shear. The spectrum for baroclinic and moisture–vortex instability would be related to how the thermal wind and the moist enthalpy gradient change the

[3] AM18 showed that moisture–vortex instability is strongest when $\tau_c \simeq 6$ h. While not shown in this study, we found that this result remains true for a two-layer QG model.

vertical tilt in a disturbance and its phase relationship with the lower-tropospheric moisture. More work is needed to show if this spectrum exists or not.

e. Similarity to the "barotropic governor" effect

The results of this study also show that moisture–vortex instability is enhanced at the expense of baroclinic instability, reminiscent to the so-called "barotropic governor" effect (James 1987). In this effect, the meridional shear in the zonal wind reduces the meridional scale of the most unstable modes, reducing the growth rate from baroclinic instability. Thus, in baroclinic regions, barotropic instability is enhanced at the expense of baroclinic instability. Similarly, the enhanced role of water vapor as τ_c increases causes the most unstable modes to shift away from the vertically tilted structure that favors baroclinic instability. This shift suggests the possible existence of a "moist governor" effect analogous to the barotropic governor, but acting on the vertical structure of the most unstable modes rather than the horizontal structure.

8. Concluding remarks

In the tropics, baroclinic instability was thought to be important over the South Asian and North African monsoons, both regions that are characterized by easterly vertical wind shear. Recent work has questioned the role of baroclinic instability in disturbances that grow in this region (Cohen and Boos 2016; Russell et al. 2020; Russell and Aiyyer 2020). Results from the simple model analyzed here supports these studies and suggests that moisture–vortex instability may be preferred in these regions instead.

It is important to recognize that the model analyzed here is highly idealized and simplified. The QG approximation may not always be applicable in AEWs and MLPSs (Boos et al. 2015). Future studies may examine idealized models that do not apply this approximation, and perhaps are more tailored to the mean state in which these systems occur. A more refined model can perhaps further elucidate what mechanism leads to the growth of MLPSs and AEWs. These refined models can also elucidate how these systems will respond to climate change (Dong et al. 2020).

Last, the gross PV equation is shown to be a useful quantity in determining the relative role of dry PV and moist enthalpy in a moist, balanced wave. Gross PV is nearly identical to the "moist" PV discussed by Lapeyre and Held (2004). Additionally, as noted by AM18, the gross PV equation bears resemblance to the precipitating QG equations discussed by Smith and Stechmann (2017), and some of the results discussed here resemble studies that use these equations (Wetzel et al. 2017, 2020). The gross PV equation also bears resemblance to the "equivalent" Ertel PV employed by some studies (Rotunno and Klemp 1985; Martin et al. 1992; Cao and Cho 1995; Marquet 2014). It is likely that gross PV is related to these other PV quantities, but a rigorous derivation showing this has not been performed. Future work will seek to elucidate the relationship between these quantities. If they are indeed related, it may be possible to develop diagnostic tools that help us improve the simulation and forecasting of systems such as MLPSs and AEWs.

Acknowledgments. ÁFA was supported by the National Science Foundation's Grant AGS-1841559. ÁFA would like to thank Yi Ming and Spencer Clark for conversations that motivated the development of the two-layer model presented here. Conversations with Anantha Aiyyer also motivated this study and prompted the discussion on the barotropic governor effect. The author also thanks three anonymous reviewers for constructive comments that improved the contents of the manuscript.

APPENDIX

Applicability and Approximate Solutions to the Linear Moist QG Model

a. Applicability of the QG approximation to MLPSs and AEWs

The applicability of the QG approximation is contingent on the Rossby number (Ro) being much smaller than unity (Ro $\ll$ 1). The Rossby number is typically written as

$$\mathrm{Ro} = \frac{\overline{u}}{f_0 L}. \tag{A1}$$

In both the South Asian and African monsoons, $\overline{u} \sim 10\ \mathrm{m\ s^{-1}}$. The zonal scale of monsoon low pressure systems has been estimated to be 2000 km (Godbole 1977; Sikka 1977; Lau and Lau 1990). Combining results yields Ro = 0.12 suggesting that the QG approximation may be applicable in this case. It is worth noting that for stronger monsoon depressions, which exhibit stronger winds and a smaller horizontal scale, the QG approximation is not necessarily applicable, as discussed by Boos et al. (2015).

Previous research has estimated the Rossby number for African easterly waves to be near 0.25 (Grist et al. 2002). African easterly waves exhibit wavelengths that range from 2000 to 5000 km and can span a wide range of latitudes, from 5° to 20°N, with centers of action both north and south of the easterly jet (Burpee 1972; Reed et al. 1977; Diedhiou et al. 1999). If we assume the center of these waves lies near 10°N, we find that the Rossby number for individual vortices ranges from 0.12 to 39. While the low end of this range would validate the use of the QG approximation, the higher range does not. While the results of this study may provide some qualitative insights about the growth of AEWs, the results may not always be valid for these waves.

b. Limiting cases of baroclinic instability

There are two limiting cases to Eq. (38) that are worth discussing.

1) Dry baroclinic instability

In a dry atmosphere, $m = 1$, which causes Eq. (38) to reduce to

$$\mathfrak{B}_d = 0, \tag{A2}$$

which yields the dispersion

$$\omega_{0d} = -\frac{\beta\left(2k^2 + k_d^2\right)}{2k\left(k^2 + k_d^2\right)} \pm \delta_d, \tag{A3}$$

where

$$\delta_d = \left[\frac{\beta^2 k_d^4}{4k^2\left(k^2+k_d^2\right)^2} - \frac{\overline{u}_T^2 k^2\left(k_d^2-k^2\right)}{k^2+k_d^2}\right]^{1/2}. \tag{A4}$$

Equation (A3) describes the propagation of waves that may grow through dry baroclinic instability if δ_d is imaginary. It is well documented that when $\overline{u}_T = 0$ Eq. (A3) yields

$$\omega_{0d}^{(1)} = -\frac{\beta}{k}, \quad \omega_{0d}^{(2)} = -\frac{\beta k}{k^2+k_d^2}, \tag{A5}$$

which describe a barotropic Rossby wave and a baroclinic Rossby wave, respectively.

2) MOIST BAROCLINIC INSTABILITY

Another limiting case worth examining is when the troposphere is saturated ($m = 0$), which yields the following dispersion relation:

$$\mathfrak{B}_m = 0. \tag{A6}$$

In such a case the wave frequency is equal to

$$\omega_{0m} = -\left(\frac{\beta}{2k} + \frac{\beta_q k}{2k_d^2}\right) \pm \delta_m, \tag{A7}$$

where

$$\delta_m = \left[\frac{\left(\beta k_d^2 - \beta_q k^2\right)^2}{4k_d^4 k^2} + \frac{\overline{u}_T k^2\left(\beta_T + \beta_q\right)}{k_d^2}\right]^{1/2}. \tag{A8}$$

We can consider two cases that elucidate the limit $m \to 0$. In the absence of a thermal wind, Eq. (A7) reduces to

$$\omega_{0m}^{(1)} = -\frac{\beta}{k}, \quad \omega_{0m}^{(2)} = -\frac{\beta_q k}{k_d^2}, \tag{A9}$$

which describe a barotropic Rossby wave and a baroclinic moisture wave. The moisture wave solution is that described by Sobel et al. (2001) in the limit of $\tau_c = 0$ and $m = 0$. It propagates due to the vortex stretching that occurs from convection that results from anomalous meridional moisture advection ($P' \propto -v_3'\partial_y \overline{q}_3$).

As in the dry baroclinic instability case, instability is possible only in the presence of a thermal wind ($\overline{u}_T \neq 0$). Recall that, even though the second rhs term in Eq. (A8) has a plus sign that $\beta_T = -\overline{u}_T k_d^2$ and $\overline{u}_T$ are of opposite signs. As a result, in the absence of β_q, the second rhs term in Eq. (A8) is always negative. Additionally, β adds a low wavenumber limit to baroclinic instability since it acts to keep the square root positive.

The contribution of β_q to instability is more complicated. The β_q can enhance instability if it is of the same sign as β_T, that is, if the temperature and moisture gradients are in the same direction. This is generally the case in the midlatitudes, where both β_q and β_T are negative, and in the South Asian summer monsoon, where they are both positive. However, if β_q and β_T are of opposite polarities then baroclinic instability is weakened. It is possible to completely eliminate baroclinic instability if β_q is of the opposite polarity as β_T and has a greater magnitude. In such a case β_m and $\overline{u}_T$ will be of the same sign and δ_m will be real for all zonal wavenumbers.

In addition to either enhancing or weakening the effectiveness of $\overline{u}_T$ in inducing baroclinic instability, β_q can also either enhance or weaken the stabilizing effect of β. If β_q is positive, the first rhs term in Eq. (A8) becomes smaller. The converse is true for a negative β_q.

3) GENERAL CASE WITH NO THERMAL WIND

In the case of no thermal wind, the solutions take the form of

$$\omega_0^{(1)} = -\frac{\beta}{k}, \quad \omega_0^{(2)} = -\frac{m\beta k + (1-m)\beta_q k}{mk^2 + k_d^2}, \tag{A10}$$

which is the barotropic Rossby wave solution and the moist Rossby wave solution described in AM18.

REFERENCES

Adames, Á. F., and D. Kim, 2016: The MJO as a dispersive, convectively coupled moisture wave: Theory and observations. *J. Atmos. Sci.*, **73**, 913–941, https://doi.org/10.1175/JAS-D-15-0170.1.

Adames, A. F., and Y. Ming, 2018a: Interactions between water vapor and potential vorticity in synoptic-scale monsoonal disturbances: Moisture vortex instability. *J. Atmos. Sci.*, **75**, 2083–2106, https://doi.org/10.1175/JAS-D-17-0310.1.

——, and ——, 2018b: Moisture and moist static energy budgets of South Asian monsoon low pressure systems in GFDL AM4.0. *J. Atmos. Sci.*, **75**, 2107–2123, https://doi.org/10.1175/JAS-D-17-0309.1.

Ahmed, F., and J. D. Neelin, 2018: Reverse engineering the tropical precipitation–buoyancy relationship. *J. Atmos. Sci.*, **75**, 1587–1608, https://doi.org/10.1175/JAS-D-17-0333.1.

——, Á. Adames, and J. D. Neelin, 2020: Deep convective adjustment of temperature and moisture. *J. Atmos. Sci.*, **77**, 2163–2186, https://doi.org/10.1175/JAS-D-19-0227.1.

Aravequia, J. A., V. B. Rao, and J. P. Bonatti, 1995: The role of moist baroclinic instability in the growth and structure of monsoon depressions. *J. Atmos. Sci.*, **52**, 4393–4409, https://doi.org/10.1175/1520-0469(1995)052<4393:TROMBI>2.0.CO;2.

Betts, A. K., 1986: A new convective adjustment scheme. Part I: Observational and theoretical basis. *Quart. J. Roy. Meteor. Soc.*, **112**, 677–691, https://doi.org/10.1002/qj.49711247307.

——, and M. Miller, 1986: A new convective adjustment scheme. Part II: Single column tests using GATE wave, BOMEX, ATEX and Arctic air-mass data sets. *Quart. J. Roy. Meteor. Soc.*, **112**, 693–709, https://doi.org/10.1002/qj.49711247308.

Boos, W. R., J. V. Hurley, and V. S. Murthy, 2015: Adiabatic westward drift of Indian monsoon depressions. *Quart. J. Roy. Meteor. Soc.*, **141**, 1035–1048, https://doi.org/10.1002/qj.2454.

Bretherton, C. S., M. E. Peters, and L. E. Back, 2004: Relationships between water vapor path and precipitation over the tropical oceans. *J. Climate*, **17**, 1517–1528, https://doi.org/10.1175/1520-0442(2004)017<1517:RBWVPA>2.0.CO;2.

Bretherton, F. P., 1966: Baroclinic instability and the short wavelength cut-off in terms of potential vorticity. *Quart. J. Roy. Meteor. Soc.*, **92**, 335–345, https://doi.org/10.1002/qj.49709239303.

Brown, R. G., and C. Zhang, 1997: Variability of midtropospheric moisture and its effect on cloud-top height distribution during

TOGA COARE. *J. Atmos. Sci.*, **54**, 2760–2774, https://doi.org/10.1175/1520-0469(1997)054<2760:VOMMAI>2.0.CO;2.

Burpee, R. W., 1972: The origin and structure of easterly waves in the lower troposphere of North Africa. *J. Atmos. Sci.*, **29**, 77–90, https://doi.org/10.1175/1520-0469(1972)029<0077:TOASOE>2.0.CO;2.

Cao, Z., and H.-R. Cho, 1995: Generation of moist potential vorticity in extratropical cyclones. *J. Atmos. Sci.*, **52**, 3263–3282, https://doi.org/10.1175/1520-0469(1995)052<3263:GOMPVI>2.0.CO;2.

Charney, J. G., 1947: The dynamics of long waves in a baroclinic westerly current. *J. Meteor.*, **4**, 136–162, https://doi.org/10.1175/1520-0469(1947)004<0136:TDOLWI>2.0.CO;2.

Chen, T.-C., J.-H. Yoon, and S.-Y. Wang, 2005: Westward propagation of the Indian monsoon depression. *Tellus*, **57A**, 758–769, https://doi.org/10.3402/tellusa.v57i5.14733.

Clark, S. K., Y. Ming, and Á. F. Adames, 2020: Monsoon low pressure system–like variability in an idealized moist model. *J. Climate*, **33**, 2051–2074, https://doi.org/10.1175/JCLI-D-19-0289.1.

Cohen, N. Y., and W. R. Boos, 2016: Perspectives on moist baroclinic instability: Implications for the growth of monsoon depressions. *J. Atmos. Sci.*, **73**, 1767–1788, https://doi.org/10.1175/JAS-D-15-0254.1.

Cook, K. H., 1999: Generation of the African easterly jet and its role in determining West African precipitation. *J. Climate*, **12**, 1165–1184, https://doi.org/10.1175/1520-0442(1999)012<1165:GOTAEJ>2.0.CO;2.

de Vries, H., J. Methven, T. H. A. Frame, and B. J. Hoskins, 2010: Baroclinic waves with parameterized effects of moisture interpreted using Rossby wave components. *J. Atmos. Sci.*, **67**, 2766–2784, https://doi.org/10.1175/2010JAS3410.1.

Diaz, M., and W. R. Boos, 2019a: Barotropic growth of monsoon depressions. *Quart. J. Roy. Meteor. Soc.*, **145**, 824–844, https://doi.org/10.1002/qj.3467.

——, and ——, 2019b: Monsoon depression amplification by moist barotropic instability in a vertically sheared environment. *Quart. J. Roy. Meteor. Soc.*, **145**, 2666–2684, https://doi.org/10.1002/qj.3585.

Diedhiou, A., S. Janicot, A. Viltard, P. de Felice, and H. Laurent, 1999: Easterly wave regimes and associated convection over West Africa and tropical Atlantic: Results from the NCEP/NCAR and ECMWF reanalyses. *Climate Dyn.*, **15**, 795–822, https://doi.org/10.1007/s003820050316.

Dong, W., Y. Ming, and V. Ramaswamy, 2020: Projected changes in South Asian monsoon low pressure systems. *J. Climate*, **33**, 7275–7287, https://doi.org/10.1175/JCLI-D-20-0168.1.

Eady, E. T., 1949: Long waves and cyclone waves. *Tellus*, **1** (3), 33–52, https://doi.org/10.3402/tellusa.v1i3.8507.

Fuchs, Ž., and D. J. Raymond, 2005: Large-scale modes in a rotating atmosphere with radiative–convective instability and WISHE. *J. Atmos. Sci.*, **62**, 4084–4094, https://doi.org/10.1175/JAS3582.1.

Godbole, R. V., 1977: The composite structure of the monsoon depression. *Tellus*, **29**, 25–40, https://doi.org/10.3402/tellusa.v29i1.11327.

Grist, J. P., S. E. Nicholson, and A. I. Barcilon, 2002: Easterly waves over Africa. Part II: Observed and modeled contrasts between wet and dry years. *Mon. Wea. Rev.*, **130**, 212–225, https://doi.org/10.1175/1520-0493(2002)130<0212:EWOAPI>2.0.CO;2.

Hannah, W. M., and A. Aiyyer, 2017: Reduced African easterly wave activity with quadrupled CO_2 in the superparameterized CESM. *J. Climate*, **30**, 8253–8274, https://doi.org/10.1175/JCLI-D-16-0822.1.

Holton, J. R., and G. J. Hakim, 2012: *An Introduction to Dynamic Meteorology*. Academic Press, 552 pp.

Hunt, K. M. R., A. G. Turner, P. M. Inness, D. E. Parker, and R. C. Levine, 2016: On the structure and dynamics of Indian monsoon depressions. *Mon. Wea. Rev.*, **144**, 3391–3416, https://doi.org/10.1175/MWR-D-15-0138.1.

Inoue, K., and L. E. Back, 2015: Gross moist stability assessment during TOGA COARE: Various interpretations of gross moist stability. *J. Atmos. Sci.*, **72**, 4148–4166, https://doi.org/10.1175/JAS-D-15-0092.1.

James, I. N., 1987: Suppression of baroclinic instability in horizontally sheared flows. *J. Atmos. Sci.*, **44**, 3710–3720, https://doi.org/10.1175/1520-0469(1987)044<3710:SOBIIH>2.0.CO;2.

Krishnakumar, V., R. N. Keshavamurty, and S. V. Kasture, 1992: Moist baroclinic instability and the growth of monsoon depressions—Linear and nonlinear studies. *Proc. Indian Acad. Sci.*, **101**, 123–152, https://doi.org/10.1007/BF02840349.

Krishnamurti, T. N., M. Kanamitsu, R. Godbole, C.-B. Chang, F. Carr, and J. H. Chow, 1976: Study of a monsoon depression (II): Dynamical structure. *J. Meteor. Soc. Japan*, **54**, 208–225, https://doi.org/10.2151/jmsj1965.54.4_208.

Kuo, Y.-H., J. D. Neelin, and C. R. Mechoso, 2017: Tropical convective transition statistics and causality in the water vapor–precipitation relation. *J. Atmos. Sci.*, **74**, 915–931, https://doi.org/10.1175/JAS-D-16-0182.1.

Lambaerts, J., G. Lapeyre, and V. Zeitlin, 2012: Moist versus dry baroclinic instability in a simplified two-layer atmospheric model with condensation and latent heat release. *J. Atmos. Sci.*, **69**, 1405–1426, https://doi.org/10.1175/JAS-D-11-0205.1.

Lapeyre, G., and I. M. Held, 2004: The role of moisture in the dynamics and energetics of turbulent baroclinic eddies. *J. Atmos. Sci.*, **61**, 1693–1710, https://doi.org/10.1175/1520-0469(2004)061<1693:TROMIT>2.0.CO;2.

Lau, K.-H., and N.-C. Lau, 1990: Observed structure and propagation characteristics of tropical summertime synoptic scale disturbances. *Mon. Wea. Rev.*, **118**, 1888–1913, https://doi.org/10.1175/1520-0493(1990)118<1888:OSAPCO>2.0.CO;2.

Mak, M., 1982: On moist quasi-geostrophic baroclinic instability. *J. Atmos. Sci.*, **39**, 2028–2037, https://doi.org/10.1175/1520-0469(1982)039<2028:OMQGBI>2.0.CO;2.

Mapes, B. E., 2000: Convective inhibition, subgrid-scale triggering energy, and stratiform instability in a toy tropical wave model. *J. Atmos. Sci.*, **57**, 1515–1535, https://doi.org/10.1175/1520-0469(2000)057<1515:CISSTE>2.0.CO;2.

Marks, F. D., Jr., and R. A. Houze Jr., 1987: Inner core structure of Hurricane Alicia from airborne Doppler radar observations. *J. Atmos. Sci.*, **44**, 1296–1317, https://doi.org/10.1175/1520-0469(1987)044<1296:ICSOHA>2.0.CO;2.

Marquet, P., 2014: On the definition of a moist-air potential vorticity. *Quart. J. Roy. Meteor. Soc.*, **140**, 917–929, https://doi.org/10.1002/qj.2182.

Martin, J. E., J. D. Locatelli, and P. V. Hobbs, 1992: Organization and structure of clouds and precipitation on the mid-Atlantic coast of the United States. Part V: The role of an upper-level front in the generation of a rainband. *J. Atmos. Sci.*, **49**, 1293–1303, https://doi.org/10.1175/1520-0469(1992)049<1293:OASOCA>2.0.CO;2.

Mass, C., 1979: A linear primitive equation model of African wave disturbances. *J. Atmos. Sci.*, **36**, 2075–2092, https://doi.org/10.1175/1520-0469(1979)036<2075:ALPEMO>2.0.CO;2.

Moon, Y., and Coauthors, 2020: Azimuthally averaged wind and thermodynamic structures of tropical cyclones in global climate models and their sensitivity to horizontal resolution.

J. Climate, **33**, 1575–1595, https://doi.org/10.1175/JCLI-D-19-0172.1.

Murthy, V. S., and W. R. Boos, 2020: Quasigeostrophic controls on precipitating ascent in monsoon depressions. *J. Atmos. Sci.*, **77**, 1213–1232, https://doi.org/10.1175/JAS-D-19-0202.1.

Neelin, J. D., and I. M. Held, 1987: Modeling tropical convergence based on the moist static energy budget. *Mon. Wea. Rev.*, **115**, 3–12, https://doi.org/10.1175/1520-0493(1987)115<0003:MTCBOT>2.0.CO;2.

——, and N. Zeng, 2000: A quasi-equilibrium tropical circulation model—Formulation. *J. Atmos. Sci.*, **57**, 1741–1766, https://doi.org/10.1175/1520-0469(2000)057<1741:AQETCM>2.0.CO;2.

Nie, J., and A. H. Sobel, 2016: Modeling the interaction between quasigeostrophic vertical motion and convection in a single column. *J. Atmos. Sci.*, **73**, 1101–1117, https://doi.org/10.1175/JAS-D-15-0205.1.

——, P. Dai, and A. H. Sobel, 2020: Dry and moist dynamics shape regional patterns of extreme precipitation sensitivity. *Proc. Natl. Acad. Sci. USA*, **117**, 8757–8763, https://doi.org/10.1073/pnas.1913584117.

Núñez Ocasio, K. M., J. L. Evans, and G. S. Young, 2020: A wave-relative framework analysis of AEW–MCS interactions leading to tropical cyclogenesis. *Mon. Wea. Rev.*, **148**, 4657–4671, https://doi.org/10.1175/MWR-D-20-0152.1.

Parker, D. J., and A. J. Thorpe, 1995: Conditional convective heating in a baroclinic atmosphere: A model of convective frontogenesis. *J. Atmos. Sci.*, **52**, 1699–1711, https://doi.org/10.1175/1520-0469(1995)052<1699:CCHIAB>2.0.CO;2.

Pavan, V., and I. M. Held, 1996: The diffusive approximation for eddy fluxes in baroclinically unstable jets. *J. Atmos. Sci.*, **53**, 1262–1272, https://doi.org/10.1175/1520-0469(1996)053<1262:TDAFEF>2.0.CO;2.

Phillips, N. A., 1954: Energy transformations and meridional circulations associated with simple baroclinic waves in a two-level, quasi-geostrophic model. *Tellus*, **6**, 273–286, https://doi.org/10.1111/j.2153-3490.1954.tb01123.x.

Raymond, D. J., and X. Zeng, 2005: Modelling tropical atmospheric convection in the context of the weak temperature gradient approximation. *Quart. J. Roy. Meteor. Soc.*, **131**, 1301–1320, https://doi.org/10.1256/qj.03.97.

Reed, R. J., D. C. Norquist, and E. E. Recker, 1977: The structure and properties of African wave disturbances as observed during phase III of GATE. *Mon. Wea. Rev.*, **105**, 317–333, https://doi.org/10.1175/1520-0493(1977)105<0317:TSAPOA>2.0.CO;2.

Roja Raman, M., V. V. M. Jagannadha Rao, M. Venkat Ratnam, M. Rajeevan, S. V. B. Rao, D. Narayana Rao, and N. Prabhakara Rao, 2009: Characteristics of the tropical easterly jet: Long-term trends and their features during active and break monsoon phases. *J. Geophys. Res.*, **114**, D19105, https://doi.org/10.1029/2009JD012065.

——, M. Venkat Ratnam, M. Rajeevan, V. V. M. Jagannadha Rao, and S. V. Bhaskara Rao, 2011: Intriguing aspects of the monsoon low-level jet over peninsular India revealed by high-resolution GPS radiosonde observations. *J. Atmos. Sci.*, **68**, 1413–1423, https://doi.org/10.1175/2011JAS3611.1.

Rotunno, R., and J. Klemp, 1985: On the rotation and propagation of simulated supercell thunderstorms. *J. Atmos. Sci.*, **42**, 271–292, https://doi.org/10.1175/1520-0469(1985)042<0271:OTRAPO>2.0.CO;2.

Russell, J. O. H., and A. Aiyyer, 2020: The potential vorticity structure and dynamics of African easterly waves. *J. Atmos. Sci.*, **77**, 871–890, https://doi.org/10.1175/JAS-D-19-0019.1.

——, ——, and J. Dylan White, 2020: African easterly wave dynamics in convection-permitting simulations: Rotational stratiform instability as a conceptual model. *J. Adv. Model. Earth Syst.*, **12**, e2019MS001706, https://doi.org/10.1029/2019MS001706.

Salvekar, P. S., L. George, and S. K. Mishra, 1986: Low level wind shear and baroclinic growth of monsoon depression scale waves. *Meteor. Atmos. Phys.*, **35**, 10–18, https://doi.org/10.1007/BF01029520.

Sanders, F., 1984: Quasi-geostrophic diagnosis of the monsoon depression of 5–8 July 1979. *J. Atmos. Sci.*, **41**, 538–552, https://doi.org/10.1175/1520-0469(1984)041<0538:QGDOTM>2.0.CO;2.

Sikka, D. R., 1977: Some aspects of the life history, structure and movement of monsoon depressions. *Pure Appl. Geophys.*, **115**, 1501–1529, https://doi.org/10.1007/BF00874421.

Smith, L. M., and S. N. Stechmann, 2017: Precipitating quasigeostrophic equations and potential vorticity inversion with phase changes. *J. Atmos. Sci.*, **74**, 3285–3303, https://doi.org/10.1175/JAS-D-17-0023.1.

Sobel, A. H., J. Nilsson, and L. M. Polvani, 2001: The weak temperature gradient approximation and balanced tropical moisture waves. *J. Atmos. Sci.*, **58**, 3650–3665, https://doi.org/10.1175/1520-0469(2001)058<3650:TWTGAA>2.0.CO;2.

——, S. Wang, and D. Kim, 2014: Moist static energy budget of the MJO during DYNAMO. *J. Atmos. Sci.*, **71**, 4276–4291, https://doi.org/10.1175/JAS-D-14-0052.1.

Sugiyama, M., 2009: The moisture mode in the quasi-equilibrium tropical circulation model. Part I: Analysis based on the weak temperature gradient approximation. *J. Atmos. Sci.*, **66**, 1507–1523, https://doi.org/10.1175/2008JAS2690.1.

Thorncroft, C. D., and B. J. Hoskins, 1994: An idealized study of African easterly waves. I: A linear view. *Quart. J. Roy. Meteor. Soc.*, **120**, 953–982, https://doi.org/10.1002/qj.49712051809.

Vallis, G. K., 2017: *Atmospheric and Oceanic Fluid Dynamics*. Cambridge University Press, 946 pp.

Wang, B., and X. Xie, 1996: Low-frequency equatorial waves in vertically sheared zonal flow. Part I: Stable waves. *J. Atmos. Sci.*, **53**, 449–467, https://doi.org/10.1175/1520-0469(1996)053<0449:LFEWIV>2.0.CO;2.

Wetzel, A. N., L. M. Smith, and S. N. Stechmann, 2017: Moisture transport due to baroclinic waves: Linear analysis of precipitating quasi-geostrophic dynamics. *Math. Climate Wea. Forecasting*, **3**, 28–50, https://doi.org/10.1515/mcwf-2017-0002.

——, ——, ——, J. E. Martin, and Y. Zhang, 2020: Potential vorticity and balanced and unbalanced moisture. *J. Atmos. Sci.*, **77**, 1913–1931, https://doi.org/10.1175/JAS-D-19-0311.1.

Yanai, M., S. Esbensen, and J. Chu, 1973: Determination of bulk properties of tropical cloud clusters from large-scale heat and moisture budgets. *J. Atmos. Sci.*, **30**, 611–627, https://doi.org/10.1175/1520-0469(1973)030<0611:DOBPOT>2.0.CO;2.

Yoon, J.-H., and T.-C. Chen, 2005: Water vapor budget of the Indian monsoon depression. *Tellus*, **57A**, 770–782, https://doi.org/10.3402/tellusa.v57i5.14737.

Yu, J.-Y., C. Chou, and J. D. Neelin, 1998: Estimating the gross moist stability of the tropical atmosphere. *J. Atmos. Sci.*, **55**, 1354–1372, https://doi.org/10.1175/1520-0469(1998)055<1354:ETGMSO>2.0.CO;2.